Three-dimensional genome architecture connects chromatin structure and function in a major wheat pathogen

Ivona Glavincheska[1] and Cecile Lorrain[1*]

[1] Plant Pathology Group, Institute of Integrative Biology, ETH Zürich, Zürich, Switzerland

*Corresponding author: cecile.lorrain@usys.ethz.ch

ABSTRACT

Background:

Genome spatial organization plays a fundamental role in biological function across all domains of life. While the principles of nuclear architecture have been well-characterized in animals and plants, their functional relevance in filamentous fungi remains largely uncharacterized. The wheat pathogen *Zymoseptoria tritici* presents a unique model for genome evolution, with a compartmentalized genome comprising conserved core and highly variable accessory chromosomes linked to genome plasticity. Here, we present the first 3D genome analysis of a eukaryotic organism with an extensive set of accessory chromosomes, revealing a hierarchical genome architecture integrating core and accessory regions.

Results:

At the nuclear level, centromere clustering defines the global genome conformation. Accessory chromosomes are spatially segregated from core arms but maintain focal contacts with pericentromeric regions of core chromosomes, contributing to mitotic stability. At finer resolution, we identify homotypic interactions among heterochromatin-rich compartments and self-interacting domains demarcated by specific histone marks, gene expression profiles, and insulator-like sequence motifs. Notably, a subset of highly insulated, transposon-rich heterochromatic domains forms strong inter-domain interactions.

Additionally, domains defined under axenic conditions with coordinated transcriptional activation during wheat infection suggest a link between 3D architecture and dynamic gene regulation.

Conclusion:

Our study uncovers the multi-scale principles of nuclear organization in a major fungal plant pathogen and reveals how hierarchical nuclear architecture contributes to gene expression coordination and genome stability. These findings establish a conceptual framework for investigating 3D genome function and chromatin-mediated regulation in filamentous fungi and other eukaryotic microbes.

KEYWORDS

3D genome architecture, chromatin interacting domains (CIDs), chromatin organization, fungal pathogen, transposable elements, epigenomics, Zymoseptoria tritici, Hi-C.

BACKGROUND

The spatial organization of eukaryotic genomes is fundamental to cellular function, underpinning chromosomal dynamics, and contributes to genome integrity and regulation [1–3]. The physical arrangement of the chromatin in the nuclear space reflects a highly ordered and dynamic hierarchical architecture. Advances in chromosome conformation capture integrated with high-throughput sequencing (Hi-C) have significantly transformed our understanding of genome organization. In addition, Hi-C combined with polymer physics models, can be used to differentiate between chromatin states and describe chromosomal conformation [4]. The comparison of 3D genome organization across the tree of life highlights both shared features and distinct aspects of genome organization between organisms, raising the question of whether common principles govern genome architecture [5].

At the largest scale, chromosomes are organized into distinct conformations within the nucleus, generally categorized into two main types: chromosome territory-like and Rabl-like organizations [2]. Chromosome territory-like organization, primarily observed in mammals, is characterized by minimal inter-chromosomal interactions, with each chromosome occupying a discrete nuclear region during interphase [2]. In contrast, Rabl-like configurations are characterized by one or more of the following features: inter-centromere clustering, inter-telomere clustering, or parallel chromosomal alignment with both centromere and telomere clustering [2]. These features are reminiscent of the classic Rabl configuration first described in mitotic cells, where centromeres and chromosome arms are arranged in parallel [6]. The distinction between territory-based and Rabl-like chromosome conformations is thought to be driven by the presence or absence of the condensin II complex [2]. Beyond these large-scale arrangements, chromatin is further organized into epigenetically distinct domains known as A and B compartments, which preferentially interact with regions of similar chromatin state [3,5,7]. In metazoan genomes, A compartments typically correspond to gene-rich, euchromatic regions associated with active

57 transcription, while B compartments are enriched in heterochromatic marks, depleted in genes, and
58 generally transcriptionally repressed. This bipartite organization reflects a fundamental level of genome
59 partitioning into functionally distinct chromatin states. In Hi-C data, these compartments are typically
60 inferred from principal component analysis (PCA) of the contact matrix, where the first eigenvector
61 separates regions with preferential self-interaction into A- or B-type compartments based on their
62 chromatin and transcriptional features [8,9]. At a finer resolution, chromatin is organized into
63 topologically associating domains (TADs), self-interacting regions within which DNA sequences interact
64 more frequently than with sequences outside the domain [8]. The function of TADs remains debated, but
65 they have been described as playing an important role in regulating gene expression, partly by modulating
66 the interactions between regulatory elements and their target genes [11–13]. TAD boundaries act as
67 insulators that constrain or mediate chromatin loop extrusion to ensure proper genomic interactions.
68 Boundaries are enriched for architectural proteins, such as the cohesin complex and the DNA-binding
69 protein CCCTC-binding factor (CTCF), and frequently coincide with regions containing highly transcribed
70 housekeeping genes [11]. The disruption of genome folding can disrupt interactions between genes and
71 regulatory elements, as observed in the enhancer hijacking of proto-oncogenes [12,13]. In contrast to
72 metazoan systems, other organisms exhibit 3D genome organization patterns that, although reminiscent
73 of features such as loops and compartments observed in mammals, arise through distinct mechanisms. In
74 plants, chromatin is arranged into self-interacting domains associated with different transcriptional and
75 epigenetic states, such as gene-active, Polycomb-repressed, and intermediate regions [8,17]. Although
76 Hi-C maps of plant genomes reveal features resembling metazoan TADs, with boundaries often enriched
77 in highly transcribed or epigenetically marked loci, plants lack orthologues of canonical architectural
78 proteins like CTCF [8,14–16]. Furthermore, in large plant genomes, genes separated by heterochromatic
79 regions frequently engage in long-range looping, suggesting a genome organization driven more by
80 structural constraints than by enhancer-promoter interactions [14,17]. Beyond eukaryotes, Hi-C

experiments in prokaryotes have revealed that bacterial and archaeal genomes are also spatially structured. In bacteria, chromosomal interaction domains (CIDs) represent nested, self-associating units that are typically demarcated by highly expressed genes [18–20]. CIDs reflect an organization principle where operon-level co-regulation may be shaped by spatial proximity. In archaea, more complex folding has been observed, including compartment-like patterns and transcriptionally linked CIDs, with boundary formation influenced by both SMC proteins and transcriptional activity [21,22]. These findings depict hierarchical 3D genome organization as a universal feature, but its underlying mechanisms and biological roles differ substantially across the tree of life. Understanding the establishment and regulatory impact of 3D genome organization is therefore essential. Yet, despite significant progress in metazoan models, these processes remain poorly understood in many other eukaryotes, particularly in fungi.

The fungal kingdom, comprising millions of species, has significant ecological and economic impacts [23]. Fungal genomes display an extraordinary range of sizes and architectures, from compact, gene-dense assemblies of under 10 Mb with very few repetitive elements, such as in *Saccharomyces cerevisiae* [24], to massive genomes exceeding 1 Gb that are dominated by transposable elements (TEs), as observed in obligate biotrophic plant pathogens where TE content can reach over 90% of the genome [25]. This variation is frequently accompanied by distinct genome compartmentalization, with some species exhibiting clear separation between gene-dense, TE-poor regions and gene-poor, TE-rich regions [26,27]. In some species, this compartmentalization extends to the chromosomal level, where dispensable accessory chromosomes are often enriched in TEs and species-specific genes [27]. Despite the remarkable genomic diversity observed across the fungal kingdom, our understanding of their 3D genome organization remains limited [28]. While certain features appear to be conserved, other aspects of nuclear architecture display substantial variability across fungal lineages, underscoring the need for broader high-resolution comparative analyses. Fungal genomes generally exhibit a Rabl-like organization characterized

105 by centromere clustering, as demonstrated in yeast and filamentous fungi [28,29]. However, the spatial
106 organization of accessory chromosomes remains completely unknown. Whether these chromosomes
107 adopt similar spatial constraints as core chromosomes or are sequestered in distinct nuclear territories is
108 currently unresolved. In addition, preferential spatial interactions among transcriptionally A and B
109 chromatin are not uniformly observed in fungi. To date, clear evidence for A/B compartmentalization has
110 been reported only in a limited number of fungal species, such as *Rhizophagus irregularis* [30]. Self-
111 interacting chromatin domains have been described in multiple fungal species using Hi-C approaches.
112 While these structures resemble TADs of metazoans or CIDs of prokaryotes, their defining features vary
113 across fungal species. In *Saccharomyces cerevisiae*, high-resolution maps revealed the presence of small
114 self-associating domains, typically covering one to five genes [31]. These domains are delimited by
115 nucleosome-depleted regions, often located at the promoters of highly transcribed genes, and are
116 enriched in chromatin remodelers and transcription factors, rather than architectural proteins [45,46]. In
117 *S. cerevisiae*, CIDs are implicated in critical genome functions such as recombination repression, genome
118 evolution, and the temporal organization of replication origins during mitosis [31]. In the filamentous
119 plant-pathogen *Verticillium dahliae*, larger domains identified as CIDs exhibit strong internal interactions
120 and are flanked by regions marked with facultative heterochromatin [32]. In *Neurospora crassa*, domain-
121 like structures consist of weakly insulated euchromatic regions interspersed with constitutive
122 heterochromatin blocks [33,34]. These findings collectively suggest that self-interacting domains are
123 widespread in fungi, but their size, boundary determinants, and chromatin context differ markedly
124 between species.

125 The fungal wheat pathogen *Zymoseptoria tritici* emerged alongside the domestication of wheat in the
126 Fertile Crescent [35]. The genome of *Z. tritici* is compartmentalized into thirteen core and eight accessory
127 chromosomes [27,36]. The core chromosomes, which are gene-rich and transposable element (TE)-poor,
128 contrast with the gene-poor and TE-rich accessory chromosomes, an ancestral feature shared across the

129 *Zymoseptoria* genus [27]. The accessory chromosomes exhibit a high degree of presence/absence
130 polymorphism in *Z. tritici* populations [37], and some chromosomes appear to be more prone to
131 destabilization than others, as indicated by targeted loss experiments [38]. The genomic partitioning of *Z.*
132 *tritici* is further reflected by distinct epigenetic signatures, particularly in the presence of specific histone
133 modifications in accessory chromosomes [39]. The epigenetic landscape of *Z. tritici* exhibits the distinction
134 of euchromatin, constitutive and facultative heterochromatin, cytosine methylation (5mC) regions, small
135 acrocentric centromeres, and telomeric repeats, underlining the complexity of *Z. tritici*'s chromatin
136 organization [27,40–45]. Cytological observations using GFP-tagged centromeres previously reported the
137 presence of 4-7 centromeric foci during interphase, suggesting partial centromere clustering [39].
138 Pathogenicity-related genes in *Z. tritici* are enriched within TE-rich regions of the genome, which likely
139 facilitates rapid evolution through genome rearrangements and epigenetic regulation [45,46]. These
140 genes are predominantly repressed in the absence of the host and maintained in a transcriptionally silent
141 state by heterochromatin marks [46]. Upon host colonization, chromatin remodeling events activate the
142 expression of pathogenicity-related genes [46]. Despite these detailed insights into the genomic and
143 epigenomic features of *Z. tritici*, the three-dimensional organization of its genome remains
144 uncharacterized. In particular, how chromatin domains are spatially arranged, whether accessory
145 chromosomes occupy distinct nuclear territories, and the extent to which point centromeres cluster
146 within the nucleus are open questions in the field. Furthermore, the presence and determinants of self-
147 interacting chromatin domains in *Z. tritici* have yet to be investigated. This study addresses these gaps by
148 integrating high-resolution Hi-C data with genomic, epigenomic, and transcriptomic information to
149 comprehensively characterize the 3D genome architecture of *Z. tritici*. To our knowledge, this represents
150 the first in-depth analysis of spatial genome organization in a eukaryotic microbe with a
151 compartmentalized genome that includes eight accessory chromosomes. By mapping the folding
152 principles of core versus accessory chromosomes, assessing centromere organization, and identifying

153 chromatin domains, our work provides new insights into the interplay between genome structure,
154 epigenetic regulation, and adaptive potential in fungal pathogens.

155 **RESULTS**

156 **The 3D genome of *Z. tritici* reveals distinct conformation patterns between core and accessory**
157 **chromosomes**
158
159 To investigate the three-dimensional (3D) genome organization of *Z. tritici* IPO323, we generated high-
160 resolution Hi-C sequencing revealing a Rabl-like architecture and previously undescribed spatial
161 segregation between core and accessory chromosomes. We performed Hi-C on two independent
162 replicates which showed high reproducibility (Pearson correlation = 0.87; 77–81% valid read pairs;
163 Supplementary Fig. S1). After merging replicates, we obtained ~19.2 million deduplicated valid read pairs
164 (Supplementary Table S1), enabling chromatin interaction detection at a minimal bin size of 3 kb. At this
165 resolution, 80% of bins on core chromosomes were supported by >1,000 contacts, with nearly complete
166 coverage at 10 kb on all chromosomes except chromosome 21 (Fig. 1A; Supplementary Table S2). As in
167 other fungi, local intrachromosomal contacts dominated the Hi-C map, yielding a strong diagonal (Fig. 1A).
168 The strongest interchromosomal contacts were enriched at centromeres and pericentromeric regions,
169 consistent with a Rabl-like conformation (observed-to-expected contact > 3.5; Fig. 1A, 1B; Supplementary
170 Fig. S2-S3). These centromeric regions were previously mapped in IPO323 using CENH3 (CENP-A homolog)
171 ChIP-seq [39] and their enrichment in inter-chromosomal contacts independently confirms their spatial
172 colocalization in the nucleus, as expected under a Rabl-like organization. Outside of centromere-
173 centromere interactions, strong interchromosomal contacts were also enriched between regions marked
174 by constitutive heterochromatin (H3K9me3; Supplementary Fig. S3; Supplementary Table S3). Notably,
175 32.6% of the strong interchromosomal interactions (observed-to-expected contact > 3.5) occurred

176 between two H3K9me3-enriched bins, revealing a heterochromatin network spanning multiple
177 chromosomes (Supplementary Fig. S3C-D).
178
179 Accessory chromosomes occupy a defined spatial niche within the nucleus, exhibiting preferential
180 associations with the pericentromeric regions of core chromosomes. Specifically, 78.6% of core-accessory
181 interactions involved contacts spanning the full length of accessory chromosomes but were restricted to
182 the pericentromeric regions of core chromosomes (observed-to-expected contact > 3.5; Fig. 1B;
183 Supplementary Fig. S3C). This spatial organization suggests that accessory chromosomes are tethered to
184 core chromosomes pericentromeric regions, while mostly remaining separated from core chromosome
185 long arms (Fig. 1B). These findings provide the first spatial insight into accessory chromosome positioning
186 in a fungal genome and support a model in which centromere-proximal anchoring contributes to higher-
187 order genome compartmentalization. Given the known instability of accessory chromosomes [38], we
188 tested whether their nuclear interactions influence their maintenance. Using log-transformed Poisson
189 regression, we found a significant negative association between interaction strength (normalized for
190 accessory chromosome size) and chromosome loss frequency following β-tubulin inhibition in IPO323 [38]
191 (p-value = 5.33e-05 for the intercept; p-value = 0.0025 for normalized interaction strength; Fig. 1D). This
192 result supports a model in which stronger core-accessory chromosome interactions correlate with
193 accessory chromosome stability.
194
195 To determine whether core and accessory chromosomes differ in their folding behavior, we estimated
196 the contact frequency decay exponent (α) as a function of genomic distance. The core chromosomes
197 exhibited an average decay exponent of α = -1.22 (standard deviation (SD) = 0.1), with three distinct
198 scaling regimes depending on genomic separation, consistent with hierarchical chromatin organization
199 (Fig. 1C; Supplementary Table S4). At short distances (< 70 kb), contact frequency decayed more gradually

200 than the global average with α = -0.71 (SD = 0.01). Interactions between 70 kb and 1 Mb followed a more
201 heterogeneous and steeper decline with α = -1.43, SD = 0.09). At distances beyond 1 Mb, contact
202 frequency declined at a slower rate relative to intermediate distances (α = -1; SD = 0.09; Fig. 1C;
203 Supplementary Table S4). This triphasic decay pattern reflects hierarchical chromatin folding, suggestive
204 of domains or compartments on the core chromosomes. In contrast, the accessory chromosomes showed
205 low difference between short- and long-distance contact frequency decay (α = -0.71 vs. α = -0.62),
206 consistent with weak or absent domain-level organization (Fig. 1C; Supplementary Table S4). This pattern
207 suggests that, compared with the core chromosomes, accessory chromosomes behave as unitary
208 compartments exhibiting weak scale-dependent folding (Fig. 1C; Supplementary Table S4).
209
210 Taken together, these results reveal fundamental differences in chromatin conformation between core
211 and accessory chromosomes in *Z. tritici*. Core chromosomes exhibit hierarchical folding, while accessory
212 chromosomes adopt a more uniform interaction profile, indicative of a compact structure with limited
213 internal compartmentalization. These structural differences, coupled with accessory chromosomes
214 preferential tethering to pericentromeric regions of core chromosomes, suggests that accessory
215 chromosomes occupy spatially constrained territories within the nucleus potentially contributing to their
216 differential mitotic stability.

217 **B chromatin compartments in *Z. tritici* engage in homotypic interactions at the intrachromosomal level**

218 To explore how 3D chromatin organization reflects functional genome partitioning in *Z. tritici*, we
219 performed eigenvector decomposition of inter- and intrachromosomal Hi-C contact maps (Fig. 2;
220 Supplementary Figs. S4-S5). At the interchromosomal level, the first eigenvector separated chromosome
221 arms, with sub-telomeric regions on both arms displaying similar profiles, indicative of Rabl-like
222 interchromosomal interactions (Supplementary Figs. S4-S5). At the intrachromosomal level, eigenvector

223 profiles captured finer-scale chromatin features and more localized and compartmentalized interaction
224 patterns (Fig. 2; Supplementary Figs. S5). Regions with negative eigenvector values exhibited strong
225 spatial self-association, consistent with compartmental segregation. These regions were enriched for
226 heterochromatic histone modifications, including H3K9me2 and H3K9me3, and depleted of euchromatin-
227 associated marks such as H3K4me2 (i.e. analogous to B compartments; Fig. 2B; Supplementary Fig. S5). In
228 contrast, positive eigenvector regions were more often associated with euchromatic features (i.e.
229 analogous to A compartments). Comparison of contact frequencies confirmed that homotypic B-B
230 interactions were predominant, while A-A interactions were comparatively weaker (Fig. 2A). This
231 asymmetry indicates that compartmentalization in *Z. tritici* is primarily driven by interactions among
232 transcriptionally silent, heterochromatic domains, rather than by the formation of discrete euchromatic
233 A compartments.
234
235 The B-compartment blocks had an average size of ~60 kb, accounting for 14.74 Mb (~36%) of the genome,
236 and were characterized by low gene density and a high density of TEs (Fig. 2C-D, Supplementary Table S6).
237 Notably, we observed a significant enrichment of retrotransposons, particularly LINEs and LTR elements
238 from the Copia superfamily (Fischer exact test BH-adjusted p-value < 0.001, Fig. 2C-E, Supplementary
239 Table S7). In contrast, the A-compartment blocks had an average length of 100 kb, spanning a total of
240 24.35 Mb, of which 80.3% are covered by genes (9,996 genes; Fig. 2C). The A compartments exhibited
241 high gene density, low TE density (4.3% of TEs), and enrichment in miniature inverted-repeat transposable
242 elements (MITEs, Fischer exact test BH-adjusted p-value < 0.001; Fig. 2C-E). Gene ontology (GO)
243 enrichment analysis in the A-compartments revealed an overrepresentation in core cellular processes
244 including translation, ribosome function, RNA binding, and intracellular non-membrane-bounded
245 organelles (FDR-adjusted p-value < 0.01; Supplementary Table S8-S9). Consistent with these observations,
246 genes and TEs within A-compartment blocks exhibited significantly higher *in vitro* expression than those

247 in B-compartment blocks (Fig. 2F), indicating that transcriptional regulation of both genes and TEs is
248 dependent on chromatin compartmentalization.
249
250 Taken together, these findings demonstrate that the genome of *Z. tritici* is partitioned into spatially
251 segregated chromatin compartments, with heterochromatic B compartments driving the overall
252 compartmentalization landscape through strong intra-compartment interactions. This compartmental
253 organization operates at the intrachromosomal level and is distinct from the global partitioning into core
254 and accessory chromosomes, underscoring the multi-layered nature of 3D genome folding in this fungal
255 pathogen.

256 **The presence of chromatin interacting domains in *Z. tritici* reveals boundaries enriched in facultative**
257 **heterochromatin and specific DNA binding motifs**

258 To determine whether the *Z. tritici* genome is organized into chromatin-interacting domains (CIDs), we
259 calculated insulation scores from Hi-C contact maps at 3 kb resolution. We identified 513 CIDs and 533
260 CID boundaries in *Z. tritici* IPO323, with an average CID length of approximately 70 kb (Supplementary
261 Table S10-12). The distribution of CIDs varied between core and accessory chromosomes, with 92% of
262 CIDs (473 CIDs) located on core chromosomes and only 8% (40 CIDs) on accessory chromosomes
263 (Supplementary Table S12). On average, CIDs on core chromosomes contained 25 genes and 6 TEs,
264 whereas CIDs on accessory chromosomes contained an average of 14 genes and 17 TEs per CID
265 (Supplementary Table S12).

266 Since CID boundaries act as insulators between domains, we identified them by detecting local insulation
267 minima and further examined whether CID boundaries exhibited specific epigenomic and genomic
268 features (Fig. 3A-B). We observed that CID boundaries were depleted of the constitutive heterochromatin
269 histone modifications H3K9me2 and H3K9me3 but enriched for facultative heterochromatin

270 modifications H3K36me3, H4K20me1, and H4K20me3 (Fig. 3B, Supplementary Fig. S6). In accessory
271 chromosomes, CID boundaries were also enriched for accessory chromosome-associated modifications,
272 H3K27me2 and H3K27me3 (Supplementary Fig. S6). In addition, CID boundaries displayed lower TE
273 density, reduced RIP-like mutational signatures, and higher gene density compared to domain interiors.
274 Despite lacking enrichment in the active transcription mark H3K4me2, genes and TEs at CID boundaries,
275 exhibited comparable expression levels to those within CIDs, and reduced variability across conditions,
276 consistent with constitutive, stable expression patterns rather than dynamic regulation (Supplementary
277 Fig. S7). To assess whether CID boundaries in *Z. tritici* are preferentially associated with conserved or
278 functionally specialized genes, we characterized the 613 genes overlapping (>50%) with boundary regions.
279 Comparative analysis across 19 *Z. tritici* reference genomes [47] revealed that only 69 of these genes were
280 conserved across all strains indicating no significant enrichment for core genes (Fisher's test, p-value =
281 0.76; Supplementary Tables S13-S15). Similarly, we did not find enrichment of specific Gene Ontology
282 (GO) terms or functional domains (Supplementary Tables S13-S15). Finally, we searched whether specific
283 DNA binding motifs were present at CID boundaries. Motif discovery analysis uncovered 35 significantly
284 enriched known and *de novo* DNA binding motifs, which clustered into nine motif groups (Supplementary
285 Table S16). Among these, one of the strongest matches showed similarity to the consensus binding motif
286 of the mammalian KRAB zinc finger protein ZNF263, a factor recently implicated in establishing insulator
287 activity at chromatin domain boundaries [48]. IPO323 has a single protein annotated with a KRAB-like zinc
288 finger domain (ZtIPO323_082310), but this protein exhibits low sequence similarity in its zinc finger
289 domains with the human ZNF263 protein, suggesting potential convergent motif recognition or functional
290 analogs with distinct primary sequences. (Supplementary Table S17).

291 Together, these results suggest that while CID boundaries in *Z. tritici* are not enriched in conserved or
292 functionally specialized genes, they exhibit distinct epigenetic and sequence signatures consistent with a
293 potential architectural role in genome organization. The enrichment of ZNF263-like motifs points to a

294 potential mechanism of boundary insulation mediated by sequence-specific binding, possibly involving
295 fungal architectural proteins.

296 **Highly insulated CIDs define chromosomal conformation, while local CID organization regulates**
297 **transcriptional dynamics during plant infection**

298 We next investigated the internal organization of CIDs to evaluate their contribution to higher-order
299 chromatin conformation and transcriptional regulation. We observed substantial heterogeneity in
300 intrachromosomal contact patterns across CIDs, with a subset displaying pronounced insulation from
301 flanking regions, hallmarks of locally compartmentalized chromatin architecture (Fig. 3C-D). To
302 systematically identify these highly insulated domains, we compared maximum insulation scores within
303 each CID to those of their flanking boundaries. CIDs with insulation strength difference exceeding the
304 genome-wide median were classified as highly insulated CIDs (HI-CIDs), while the remainder were
305 designated as regular CIDs (R-CIDs). This analysis yielded 105 HI-CIDs, representing 20% of all CIDs
306 genome-wide (Supplementary Table S18). Analysis of strongest interactions (observed-to-expected
307 intrachromosomal contacts > 1.75) revealed significantly higher interaction frequencies between HI-CIDs
308 compared to R-CID/R-CID and HI-CID/R-CID combinations (Mann-Whitney p-value < 0.05; Supplementary
309 Fig. S8), indicating that HI-CIDs form a distinct interaction network within the genome. In addition, HI-CIDs
310 were characterized by enrichment in heterochromatin-associated histone marks (notably H3K9me2 and
311 H3K9me3), and a relative depletion of active and facultative chromatin modifications (Fig. 3C-D).
312 Consistent with their chromatin profile, HI-CIDs exhibited elevated TE density, reduced gene content, and
313 low transcriptional activity under *in vitro* conditions (Supplementary Fig. S9). Notably, HI-CIDs were also
314 enriched in predicted effector genes, implying that heterochromatin dynamics within these regions may
315 be restructured to enable effector gene activation during host infection (Fisher's exact p-value < 0.01;
316 odds ratio = 1.54; Supplementary Tables S19).

317 To investigate whether CID organization could influence co-expression patterns in *Z. tritici*, we analyzed
318 transcriptomic data obtained from both axenic culture and four stages of wheat infection. We specifically
319 asked whether genes and TEs located within the same CID (i.e. defined based on Hi-C data from axenic
320 culture) exhibit coordinated expression changes across these distinct conditions. Using a linear model, we
321 tested whether CID membership could explain patterns of differential expression between *in vitro* and *in*
322 *planta* conditions (Supplementary Tables S20–S23). The model significantly outperformed a null
323 expectation (likelihood ratio test p-value < 0.01) and explained between 5% and 9% of the adjusted
324 variance in gene and TE expression (Supplementary Table S24), indicating that CID organization may
325 contribute to transcriptional dynamics during infection. To further assess the relative contribution of CID
326 organization to transcriptional variation, we extended our linear regression model to include gene GC
327 content and distance to the nearest TE as additional predictors. Including these variables alongside CID
328 membership modestly improved the model's explanatory power, increasing the proportion of variance
329 explained by an additional 3% to 6% (Supplementary Table S24). However, in the absence of CID
330 membership as a predictor, gene GC content and TE proximity alone accounted for less than 0.1% of the
331 observed transcriptional variance, reinforcing the importance of domain-level chromatin organization in
332 regulating gene expression.

333 To identify specific CIDs exhibiting coordinated transcriptional behavior, significant CIDs from the linear
334 regression were classified as co-regulated for CIDs containing at least 10 genes and TEs. This analysis
335 revealed 46 co-regulated CIDs (8.9% of all CIDs) that exhibited significant coordination during at least one
336 stage of infection (Supplementary Fig. S10; Supplementary Table S25). Notably, 23 of these CIDs had
337 coordinated expression observed only during a single infection phase, suggesting that dynamic chromatin
338 restructuring may contribute to phase-specific transcriptional responses. A substantial fraction of co-
339 regulated domains localized to regions with accessory-like features, including 19 on accessory
340 chromosomes and six on the long arm of chromosome 7, which is enriched in H3K27me3 and exhibits low

341 gene density (Supplementary Fig. S11). Additionally, 16 of the 46 co-regulated CIDs were classified as
342 highly insulated (HI-CIDs), further linking chromatin insulation and domain architecture to coordinated
343 regulation. Collectively, these results show that a subset of CIDs functions as co-regulatory units in *Z.*
344 *tritici*, and that heterochromatic features, insulation strength, and chromosomal context together shape
345 transcriptional coordination during host infection.

346 **DISCUSSION**

347 Our study provides the first comprehensive characterization of the hierarchical 3D chromatin organization
348 in the major fungal wheat pathogen *Z. tritici*. The genome of *Z. tritici* adopts a Rabl-like nuclear
349 conformation, consistent with other fungal genomes [30,32,34,49,50] but with distinct folding patterns
350 between core and accessory chromosomes. Accessory chromosomes are anchored to the pericentromeric
351 regions of core chromosomes, with interaction strength correlating with stability, indicating that
352 pericentromeric association may reinforce their nuclear positioning and stability. We detected
353 hierarchical folding within core chromosomes, while accessory chromosomes displayed a more uniform
354 organization. Beyond this global architecture, we identified intrachromosomal compartments, with B
355 compartments engaging in homotypic interactions and enriched for retrotransposons. Furthermore, we
356 detected self-interacting CID structures with boundaries enriched in facultative heterochromatin marks,
357 stable gene expression and putative insulator motifs that resemble the binding sites of a mammalian
358 architectural protein. Additionally, we defined highly insulated CIDs that form an interaction network of
359 heterochromatic islands and harbor genes related to pathogenicity. A subset of CIDs showed
360 transcriptional co-regulation patterns that varied across infection stages, indicating a regulatory role for
361 CID organization in infection stage-specific gene expression. Our results establish a multilayered view of

362 3D genome organization in *Z. tritici*, revealing chromatin conformation as a key component of genome
363 function.

364 The core-accessory genome compartmentalization of *Z. tritici* extends beyond linear genome
365 characteristics and is mirrored in the three-dimensional organization of the nucleus. Within this nuclear
366 context, accessory chromosomes are preferentially associated with the pericentromeric regions of core
367 chromosomes while remaining excluded from interactions with core chromosome arms. Interestingly, the
368 accessory chromosomes harboring the weakest interactions with core chromosomes, specifically their
369 pericentromeric regions, were also the ones most frequently lost following treatment with carbendazim,
370 a fungicide that disrupts β-tubulin polymerization and impairs mitotic spindle assembly [38,51]. This
371 observation suggests that robust pericentromeric tethering may play a stabilizing role for accessory
372 chromosomes during mitosis. Similar phenomena have been observed in *S. cerevisiae*, where
373 microtubule-disrupting agents reduce centromere clustering, implying that centromeres are bundled at
374 the spindle pole body during interphase [52,53]. These parallels suggest that centromeric architecture in
375 *Z. tritici* may serve a comparable stabilizing function. Further supporting this hypothesis, accessory
376 chromosomes with stronger pericentromeric associations, such as chromosome 19, exhibited greater
377 stability under carbendazim treatment [38]. This chromosome also shows high prevalence in natural
378 populations of *Z. tritici* [37], aligning spatial stability with evolutionary persistence. In contrast, despite
379 the general presence/absence polymorphism trend among accessory chromosomes, those most
380 frequently lost under experimental conditions were not necessarily the least prevalent in global
381 populations [37,44]. One possible explanation for this discrepancy is that the strength of core-accessory
382 chromosome interactions may be strain-specific. It is likely that in different natural strains of *Z. tritici*, the
383 core-accessory interactions may vary, affecting the stability and presence of accessory chromosomes in a

384 context-dependent manner. Additionally, evolutionary pressures and local adaptation may influence the
385 retention or loss of these chromosomes, contributing to the observed diversity in the presence of
386 accessory chromosomes across strains [38]. Further research, including multiple-strain Hi-C analyses,
387 could provide insights into how core-accessory chromosome interactions have shaped the genomic
388 architecture of *Z. tritici*.

389 *Z. tritici* genome displays a global Rabl-like organization. Cytological observations using GFP-tagged CENH3
390 further support the Rabl-like nuclear organization, revealing that *Z. tritici* centromeres cluster into 4 to 7
391 distinct nuclear foci per nucleus during interphase [39]. These chromocenters were observed in individual
392 spores, indicating variability in centromere clustering from cell to cell. In contrast, our Hi-C data reflect an
393 averaged pattern of centromere-centromere interactions across a spore population, revealing a
394 consistent signal of clustering. The convergence of these single-cell and population-level datasets suggests
395 that while the number and position of chromocenters may vary between nuclei, centromeres consistently
396 associate into a limited number of foci, collectively shaping a Rabl-like nuclear architecture. Beyond this
397 centromere-driven global organization, the Hi-C data also reveal fine-scale compartmentalization within
398 chromosomes. Notably, the B compartments exhibit strong homotypic interactions, forming a spatially
399 distinct subnetwork largely insulated from the euchromatic A compartments, showing minimal inter-
400 compartment connectivity. Unlike the well-defined A/B compartmentalization observed in the human
401 genome [3] or the checkerboard interaction patterns reported in *R. irregularis* [30], *Z. tritici* displays a
402 genome topology that is dominated by internal B-B interactions. Compartmentalization inferred through
403 principal component analysis of Hi-C contact matrices revealed that B compartments are small (~60 kb),
404 with a similar size and positioning of CIDs identified in our study. Specifically, these B compartments co-
405 localize with highly insulated CIDs that form an interlinked network of heterochromatic regions. This

406 suggests that *Z. tritici* chromatin exhibit a heterochromatin-driven architecture, where B compartments
407 and highly insulated CIDs act as spatial reservoirs for transcriptionally repressed, TE-rich genomic regions.
408 This compartmentalization likely reinforces silencing by sequestering these regions away from the
409 transcriptionally active A compartments. Such an arrangement parallels chromatin architectures observed
410 in other fungi [30,32,49]. For example, in *N. crassa*, heterochromatic domains marked by H3K9me3
411 aggregate into discrete chromatin regions that contribute to genome stability [33,54]. In *Z. tritici*, the co-
412 occurrence of small B compartments with CID structures supports a fine-scale, heterochromatin-driven
413 genome topology that enables both regulatory insulation and structural organization.

414 We identified CIDs with specific epigenetic characterization of their boundaries, supporting the presence
415 of chromatin-interacting domains as a universal genomic feature [55]. *Z. tritici* displays CIDs of ~70 kb in
416 size, similar to the average CID size described in other fungi [32,49], but far smaller than metazoan TADs,
417 which typically span over megabases [55]. The detection of CIDs in *Z. tritici* was further supported by
418 analysis of contact probability decay slopes consistent with expectations from polymer physics modeling.
419 These patterns, showing elevated interaction frequencies at sub-100 kb distances, are consistent with the
420 presence of interaction domains [4]. Unlike TADs described in metazoans, we counted only a subset of co-
421 regulated CIDs, suggesting that structural features of the genome coordinate local transcriptional
422 regulation during host-pathogen interactions, similar to other plant-associated fungi [32,49]. In
423 metazoans, the concept of TADs is also strongly linked to the active loop extrusion creation process, which
424 is dependent on cohesin and the boundary-associated protein CTCF, or other insulator proteins [56].
425 However, self-interacting domains across the tree of life were described in the absence of insulator
426 proteins, as well as cohesin [57,58]. For instance, CIDs in prokaryotes structure the genome at the gene
427 operon level, with insulated boundaries associated with highly expressed genes [19,20,59]. In *Z. tritici*, CID

428 boundaries are gene-dense, TE-poor, and enriched in facultative heterochromatin histone modifications,
429 consistent with boundaries described in *V. dahliae* [32]. Gene expression analysis further revealed that
430 genes at CID boundaries are not markedly different in expression level compared to those within domains,
431 but display reduced expression variability and consistent expression across conditions. This pattern
432 supports a model where boundary-associated genes are constitutively expressed, in line with boundary
433 behavior in other species [32,60]. In *N. crassa*, interspersed heterochromatin blocks have been proposed
434 to act as domain boundaries in place of insulator proteins [29,33]. However, our findings in *Z. tritici*
435 suggest a more nuanced organization, as we observed multiple CIDs between heterochromatic blocks,
436 with well-defined boundaries marked by distinct epigenetic profiles that are similar to those in *V. dahliae*
437 [32]. Furthermore, we observed a significant enrichment of zinc finger transcription factor DNA-binding
438 motifs at *Z. tritici* domain boundaries, notably those associated with the vertebrate insulator protein
439 ZNF263 [61]. In *V. dahliae*, boundary-enriched GAAG-motifs and TATA-motifs associate with a decrease in
440 chromatin accessibility [32]. The presence of a zinc-finger binding motifs in *Z. tritici* CID boundaries
441 suggests that zinc-finger proteins may contribute to domain boundary formation in fungi. As a diverse and
442 underexplored protein family, zinc-finger proteins could represent architectural factors, with implications
443 for understanding genome organization.

444 Globally, CID structures exhibit low insulation scores in *Z. tritici*, consistent with previous observations in
445 other fungi [32]. However, we identified a subset of highly insulated domains (HI-CIDs) that coincide with
446 TE-rich, heterochromatic regions. Similar patterns have been described in *V. dahliae* and *Epichloë*
447 *festucae*, where accessory genomic regions (AGRs) form structurally distinct and functionally specialized
448 chromatin domains with stronger local interactions compared to surrounding regions [32,49]. In *Z. tritici*,
449 these HI-CIDs also engage more frequently in strong interactions with one another compared to R-CIDs,

450 which seems reminiscent of the spatial network formed by the "TAD cliques" observed in the human
451 genome, where clusters of heterochromatic domains co-localize in 3D space [62]. Comparable chromatin
452 bundling mechanisms have also been described in *C. elegans*, where H3K9me3 promotes chromosome
453 compaction via HP1-mediated heterochromatin interactions [63]. In *N. crassa*, interspersed
454 heterochromatin blocks are described to function as boundaries, structuring CIDs. Targeted removal of a
455 heterochromatic block induces localized architectural changes with minimal effects on fitness [54]. The
456 heterochromatin interaction network in *Z. tritici* shares conceptual similarities with the KNOT Engaged
457 Elements (KNOTs) described in *Arabidopsis thaliana* [64]. KNOTs are heterochromatic islands within
458 euchromatin that interact both within and between chromosomes. Notably, TEs preferentially insert into
459 these regions, and under heat stress, KNOT-associated TEs are derepressed, demonstrating that these
460 structures are dynamic and functional in TE regulation [65]. Previous studies in *Z. tritici* have shown that
461 wheat infection is accompanied by a global activation of TEs and epigenetic changes [46]. We found that
462 HI-CIDs are enriched for effector genes, and some of these CIDs are co-regulated *in planta,* suggesting
463 potential de-repression of HI-CIDs during infection. While our study relies on *in vitro* Hi-C data, we
464 recognize that host-induced chromatin remodeling likely plays a role in shaping 3D genome organization
465 during plant infection. The low fungal biomass during early colonization stages currently limits the
466 feasibility of generating *in planta* Hi-C maps in *Z. tritici*. Nonetheless, our finding that a subset of genes
467 and TEs located within the same *in vitro*-defined CID tend to exhibit coordinated expression changes
468 between axenic culture and infection suggests that CIDs may serve as functional domains of
469 transcriptional co-regulation. Similar observations were drawn from studies in other fungal pathogens
470 such as *V. dahliae* and *E. festucae*, where a subset of CIDs identified under axenic conditions showed
471 regulatory relevance *in planta* [32,49]. These comparisons support the broader concept that core features

472 of 3D genome architecture may be maintained across environmental conditions and can serve as
473 predictive scaffolds for gene regulation. Future efforts to develop *in planta* approaches in fungal
474 pathogens will be essential to directly validate this model and dissect the dynamics of chromatin folding
475 during host colonization. Although the mechanisms and dynamics of chromatin folding during host
476 colonization remain largely uncharacterized in fungi, the presence of specialized 3D genome organization
477 represents an evolutionary strategy to compartmentalize potentially disruptive genomic elements while
478 preserving their accessibility for regulated expression under specific developmental or stress-related
479 conditions.

480 **CONCLUSION**

481 The fundamental principles of genome folding, such as compartmentalization and domain organization,
482 are broadly conserved across eukaryotes, even if the canonical definitions developed in metazoan systems
483 do not always apply uniformly across the tree of life [55]. In the fungus *Z. tritici*, we uncovered a complex,
484 multilayered chromatin architecture characterized by centromere clustering, spatial segregation between
485 core and accessory chromosomes, a long-range heterochromatin network, and chromatin interacting
486 domains. Together, these features likely contribute to this species' remarkable genome plasticity,
487 facilitating regulatory flexibility, adaptive potential, and pathogenicity. By generating a high-resolution
488 map of *Z. tritici*'s 3D genome, we lay the groundwork for mechanistic investigations into how chromatin
489 structure governs gene expression, transposable element dynamics, and genome evolution in filamentous
490 fungi. More broadly, this work advances the emerging field of comparative 3D genomics in non-model
491 species, opening new avenues for exploring genome architecture as a driver of fungal adaptation and
492 plant-pathogen interactions.

493 **METHODS**

494 **Sample preparation and Hi-C sequencing**

495 The reference strain *Z. tritici* IPO323 [36] was preserved in 50% glycerol at -80°C. Pre-cultures were
496 prepared with inoculations of ~100uL of glycerol stock spore suspension onto solid YMS medium (4 g/L
497 yeast extract, 4 g/L malt extract, 4 g/L sucrose, and 12 g/L of agar) and grown for 4 days at 18°C. Spores
498 were scraped from plates and re-suspended into PBS buffer (8g/L NaCl, 1.44g/L Na_2HPO_4, 0.2g/L KCl,
499 0.24g/L KH_2PO_4) for sample preparation for epigenomics sequencing as described in Möller et al. 2023
500 [41]. Spores were fixed with formaldehyde according to PhaseGenomics instructions (Seattle,
501 Washington, USA). Hi-C experiments were performed with the Phase Genomics Proximo Hi-C Kit (Fungal),
502 which combines four restriction enzymes to ensure homogeneous digestion at AT-rich genomic regions.
503 The resulting libraries were sequenced at Biomarker Technologies GmbH (BMKgene, Münster, Germany).
504 The sequencing was performed with Illumina NovaSeq X, paired-end 150bp reads. Sample preparation,
505 Hi-C experiment, and sequencing were performed for two independent replicates.

506 **Hi-C data processing, binning, and visualization**

507 Each Hi-C read-pairs was filtered and trimmed using Trimmomatic v0.39 [66] with the following settings
508 ILLUMINACLIP:${adapters}:2:30:10 LEADING:15 TRAILING:15 SLIDINGWINDOW:5:15 MINLEN:50. We
509 used HiCUP-0.9.2[67] to evaluate the quality of each Hi-C dataset. Reads were mapped against the
510 reference genome assembly of *Z. tritici* IPO323 [36] using bwa-mem2 [68]. The construction and analysis
511 of Hi-C interaction matrices were performed using the HiCExplorer suite of tools [60]. Each replicate
512 interaction matrix was created using *hicBuildMatrix*, by aligning the paired reads to the reference genome
513 digested *in silico* with the four restriction enzymes DpnII (GATC), DdeI (CTNAG), HinfI (GANTC), and MseI
514 (TTAA). Contact matrices were individually corrected using the iterative correction and eigenvector
515 decomposition (ICE) method via the *hicCorrectMatrix* function. The corrected contact matrices from the

516 two biological replicates were combined to generate Hi-C matrices at 1 kb, 3 kb, 10 kb, and 50 kb. The Hi-
517 C contact maps were generated with *hicPlotMatrix*. To identify the most significant chromatin
518 interactions, we normalized the raw Hi-C contact matrices using the *hicTransform* from the HiCExplorer
519 suite with the default --method obs_exp option. This method computes expected interaction frequencies
520 as a function of genomic distance to account for the natural decay in contact frequency with increasing
521 genomic separation. The most significant pairwise interactions were extracted by filtering the observed-
522 over-expected values above 3.5 for inter- and 1.75 for intra-chromosomal interactions. The interaction
523 link plots were generated using Circos-0.69 [69]. The HiCExplorer .h5 contact matrix files were converted
524 into .cool format with *hicConvertFormat* for compatibility with the *cooltools* and *cooler* packages for
525 visualization [70]. All scripts for the analyses and visualization are available at
526 https://github.com/lorraincecile/Hi-C_Ztritici_IPO323 and 10.5281/zenodo.15395556.

527 **Estimation of chromatin folding patterns with contact probability decay**

528 To characterize chromatin folding behavior, we computed the decay of contact frequency as a function of
529 genomic distance, a method grounded in polymer physics models of chromosome organization [4]. These
530 models typically distinguish between different chromatin configurations based on the decay exponent (α)
531 of the contact probability P(s), where *s* represents genomic separation. Contact decay slopes provide
532 insights into the folding state of the chromatin (referred as "globule"): an exponent of ~1.5 corresponds
533 to an equilibrium globule, indicative of tightly knotted, inaccessible chromatin; values between 1 and 2
534 reflect a fractal globule, a compact yet unknotted state; and exponents < 1 are characteristic of a tension
535 globule, normally associated with finer scale self-interacting domain units [71]. We used the
536 *cooltools.expected_cis* [70] function to compute the average contact probability, P(s), separately for core
537 and accessory chromosomes. Genomic distances and P(s) values were transformed to log10 scales, and a

538 linear regression was fitted to the resulting log–log data to estimate the decay exponent (α), which serves
539 as a proxy for the underlying chromatin folding state.

540 **Statistical Analysis of Chromosome Loss and Interaction Strength**

541 To investigate the relationship between chromosome loss and interaction strength in *Z. tritici* IPO323, we
542 extracted the average number of core-accessory chromosome strong interactions (observed vs. expected
543 > 3.5), normalized by the size of the corresponding accessory chromosome. This normalization yielded the
544 interaction strength per accessory chromosome. We compared this measure to the frequency of
545 accessory chromosome loss following beta-tubulin inhibition, described in Habig et al. (2017) [38]. A log-
546 transformed Poisson regression model was used to assess the impact of normalized interaction strength
547 on accessory chromosome loss. The model was fitted using the glm function in R (version 4.4.1), with
548 chromosome loss modeled as a Poisson-distributed response variable. The coefficients were tested for
549 statistical significance using z-tests, with p-values calculated for both the intercept and the normalized
550 interaction strength variable. Model diagnostics, including overdispersion testing using the *dispersiontest*
551 function from the AER package [72], confirmed that the Poisson distribution was an appropriate fit. The
552 fitted model was then used to predict chromosome loss, and the observed versus predicted values were
553 visualized with ggplot2 [73].

554 **A/B compartmentalization analysis**

555 Compartmentalization analysis used the matrix at 3 and 10 kb resolution with functions from the cooltools
556 package [70]. We calculated PCA eigenvectors for intra- and inter-chromosomal contacts as *expected_cis*
557 and *expected_trans,* respectively. Eigenvector values capture spatial segregation, with regions sharing
558 similar values displaying more frequent contacts with one another than with regions showing dissimilar
559 values. The intrachromosomal eigenvector profiles capture finer-scale chromatin features and reflects

560 more local variability between contacts of the same chromosomes. GC content was used as a phasing
561 track to orient the eigenvector values. The first three eigenvector values were manually checked, and the
562 first eigenvector was determined to have the best compatibility with the interaction pattern of the contact
563 maps. We used the 2.5% and 97.5% percentile eigenvector values as the minimum and maximum range
564 to calculate the compartmentalization strength. The compartmentalization plot was generated using the
565 *saddleplot* function [70].

566 **Chromatin interacting domains (CID) calling**

567 We established 3 kb as the smallest bin size at which at least 1000 reads covered 80% of bins for each
568 chromosome [9], and therefore the smallest scale at which we can reliably call CIDs (Supplementary Table
569 S2). CID predictions were then generated using *hicFindTADs* for HiCExplorer [60] with default parameters
570 using the contact matrix at 3kb bin size. This function calculates the insulation score by evaluating
571 interaction frequencies between adjacent bins. CID boundaries were identified at significant local minima
572 in physical interactions, where large differences between adjacent bins yield negative insulation scores,
573 indicating “strong" insulation [60]. To assess the robustness of the predicted CIDs, we compared intra-
574 domain interaction frequencies within annotated domains to those calculated in size-matched regions
575 shifted upstream or downstream by half the length of each CID. All interaction values were ICE-
576 normalized. We found that the original CIDs exhibited significantly higher intra-domain contact
577 frequencies than both upstream- and downstream-shifted regions (Mann-Whitney U test; upstream: p-
578 value < 0.05; downstream: p-value < 0.05), while the difference between upstream and downstream
579 controls was not significant (p-value = 0.87) (Supplementary Fig. S12). CIDs were classified into “regular”
580 (R-CIDs) and “high insulation” (HI-CIDs) CIDs by calculating the difference between each CID’s maximum
581 insulation score and the minimum insulation scores of its adjacent CIDs. CIDs with a score difference

582 within the 20th quantile, insulation scores above the median, and flanked by two neighboring CIDs with
583 negative insulation scores were considered HI-CIDs.
584
585 **Analysis of genomic features**
586 Gene annotations with associated GO terms, PFAM and effector predictions were sourced from Lapalu et
587 al. (2023) [74] and accessible here (https://bioinfo.bioger.inrae.fr/portal/genome-portal/12/).
588 Centromere detections and annotations were sourced from Schotanus et al. (2015), where centromere
589 positions were experimentally determined using chromatin immunoprecipitation followed by sequencing
590 (ChIP-seq) targeting the centromere-specific histone H3 variant CENH3 (CENP-A homolog) [39]. Core
591 genes were identified as described in Minana-Posada et al. (2024)[75] as shared across 19 *Z. tritici* strains
592 [47]. GO term enrichment analysis was performed using *topGO*'s *runGOEnrichment* function [76]. GO
593 terms with no gene associations in the query lists or supported by only a single gene across the genome
594 were excluded. False discovery rate (FDR) correction was applied to all p-values. Enrichment analyses of
595 effectors, core genes, and PFAM domains within gene sets were performed using Fisher's exact tests, with
596 FDR correction applied to *p*-values. TE annotations were obtained from the manually curated library of
597 Baril and Croll (2023) [77]. CID boundary motif identification and enrichment were performed with
598 XSTREME with default parameters and compared to JASPAR database motifs [78] using Tomtom from the
599 MEME suite tools [79]. We used the RIP composite index to identify RIP-like signatures in 1 kb sliding
600 windows across the genome as described in Lorrain et al. (2021) [45]. A positive RIP composite index value
601 reflects the presence of RIP-like mutations. The distribution of genes, TEs and RIP-like signatures across
602 CIDs and their boundaries was analyzed using the EnrichedHeatmap package in R [80].

603 **Gene and TE expression analyses**

604 RNA-seq data for *Z. tritici* IPO323 during *in planta* infection, comprising four distinct infection stages, was
605 obtained from Haueisen et al. (2018) [81], while *in vitro* RNA-seq data was sourced from Möller et al.
606 (2023) [41]. After trimming low-quality reads (ILLUMINACLIP:${adapters}:2:30:15 MINLEN:100), the
607 resulting high-quality reads were aligned to the IPO323 reference genome using STAR [82], with
608 parameters configured to allow the inclusion of multimapping reads (--outFilterMultimapNmax 200 and
609 –winAnchorMultimapNmax 200). To capture the expression of genes and TEs, multi-mapper reads were
610 reassigned using TEtranscript [83], which ensures precise allocation of reads to the transcript sequences
611 [74] (https://bioinfo.bioger.inrae.fr/portal/genome-portal/12/) and TE library of *Z. tritici* IPO323 [77].
612 Differential expression analysis was performed using DESeq2 [84], comparing expression levels across the
613 biotrophic phases (stages A and B), necrotrophic phases (stages C and D) [81], and *in vitro* growth
614 conditions. To compare transcription between boundaries and CIDs, genes and TEs were analyzed
615 separately, and statistical comparisons of expression levels and fold-change distributions were performed
616 using two-sided Mann-Whitney U tests. The distribution of expression levels *in vitro* ($\log_2$ RPKM) and
617 differential expression comparing axenic and *in planta* conditions ($\log_2$ fold-change), across CIDs and their
618 boundaries, was analyzed using the EnrichedHeatmap package in R [80]. For each gene or TE, $\log_2$-
619 transformed values were calculated and centered on CID boundaries, extending 35 kb upstream and
620 downstream. Heatmaps display normalized expression values per element, and the average signal profile
621 across all regions is plotted above each heatmap. Absolute $\log_2$ fold-change values were used to assess
622 expression stability across conditions.

623 **Characterization of epigenetic profiles**

624 Histone modifications, centromere detection, and cytosine DNA methylation (5mC) level enrichments
625 across the *Z. tritici* IPO323 genome were assessed using publicly available chromatin immunoprecipitation

626 followed by sequencing (ChIP-seq) and whole-genome bisulfite sequencing (WGBS) datasets. ChIP-seq
627 datasets for CenH3 and H3K9me2 were obtained from Schotanus et al. (2015) [39], while datasets for
628 H3K36me3, H4K20me3, H4K20me1, H3K27me3, H3K27me2, and H3K4me2 were sourced from Möller et
629 al. (2023) [41]. Reads were preprocessed using Trimmomatic v0.39 [66], with parameters
630 ILLUMINACLIP:${adapters}:2:30:10 LEADING:3 TRAILING:3 SLIDINGWINDOW:4:15 MINLEN:30 and
631 ILLUMINACLIP:${adapters}:2:30:10:2:keepBothReads HEADCROP:5 LEADING:3 TRAILING:3
632 SLIDINGWINDOW:4:15 MINLEN:30 for the single and paired end samples respectively. The filtered reads
633 were mapped to the IPO323 reference genome using Bowtie2 with default settings [85]. To account for
634 the repetitive nature of TEs in the genome, multimapping reads were subsequently mapped using Allo
635 [86], an approach tailored to improve mapping accuracy in repeat-rich regions. Reads with a mapping
636 quality score below 30 and PCR duplicates identified by Picard v2.26.2 [87] were excluded from further
637 analysis. To visualize enrichment levels across the genome, histone enrichment profiles were generated
638 as bigWig and bedGraph files in bins of 10 bp, 3 kb, and 10 kb.
639 Bisulfite sequencing data was retrieved from Möller et al. (2021) [42] for cytosine DNA methylation
640 analysis. Cultures were inoculated directly from glycerol stocks into liquid YMS medium and grown for 5
641 days. The Illumina HiSeq3000 paired-end raw reads were filtered using Trimmomatic [66] parameters
642 HEADCROP:10 CROP:140 LEADING:3 TRAILING:3 SLIDINGWINDOW:4:15 MINLEN:50 and subsequently
643 mapped and deduplicated using Bismark [88]. The methylated sites in all contexts (CG, CHG, CHH) were
644 extracted using the function *bismark_methylation_extractor,* and filtered to remove sites not supported
645 by at least four reads and more than 50% of the mapped reads. The weighted methylation average was
646 calculated for 10 bp, 3 kb and 10 kb windows. The distribution of histone marks and 5mC levels across
647 CIDs and their boundaries was analyzed using the EnrichedHeatmap package in R [80].

648 **Chromatin interacting domains co-expression analysis**

649 To investigate the co-regulation of genes and TEs within CIDs, we constructed a linear model in Python
650 as described in Winter et al. (2018) [49]. The model utilized the log2-fold change in gene expression
651 between *in planta* and *in vitro* stages as the response variable, with CID membership as the main
652 predictor. We developed nested models by incorporating additional genomic features known to affect
653 gene expression, including GC content and distance to the nearest TE. The nested models' performance
654 was evaluated using the Akaike Information Criterion (AIC) and likelihood ratio tests. We defined CIDs as
655 co-regulated CIDs with more than 10 co-expressed genes and TEs. **Code availability**

656 All custom scripts generated for data analyses and visualization are available at
657 https://github.com/lorraincecile/Hi-C_Ztritici_IPO323. The Hi-C contact matrices and CID annotations as
658 well as source data for figures and tables presented in this study are available at
659 10.5281/zenodo.15395556.

660 **Data availability**

661 The Hi-C sequencing data is publicly available from the NCBI Gene Expression Omnibus (GEO) under the
662 accession GSE296663. *In planta* [81] and *in vitro* [41] RNA-seq datasets are available at the GEO accession
663 number GSE106136 and the accession number NCBI BioProjects PRJNA902413, respectively. The ChIP-seq
664 datasets for CenH3 and H3K9me2 [39] are accessible through the SRA ID SRP059394. The ChIP-seq
665 datasets for H3K36me3, H4K20me3, H4K20me1, H3K27me3, H3K27me2, and H3K4me2 [41] are available
666 at the SRA ID SRP411885. Whole-genome bisulfite sequencing [42] data are available at SRA under
667 BioProject ID PRJNA614493.

668 **Authors contributions**

669 IG and CL designed the experiments. IG performed data acquisition. IG and CL performed the data analysis
670 and interpretation. CL conceptualized the study. IG and CL wrote and revised the manuscript.

671 **Funding Declaration**

672 Ivona Glavincheska and Cecile Lorrain are funded by a SNSF Ambizione grant (PZ00P3_209022).

673 **Acknowledgments**

674 We thank Prof. Bruce McDonald and ETH Zurich for funding the Hi-C sequencing. We thank Dr. Mareike
675 Möller for her advice on performing Hi-C experiments in filamentous fungi.

676 **AI language model assistance**

677 We used ChatGPT (developed by OpenAI) to refine and improve the grammar of the text. We reviewed
678 and revised all outputs to ensure accuracy and alignment with the intended message.

679 **ETHICS DECLARATIONS**

680 **Ethics approval and consent to participate**

681 Not applicable.

682 **Consent for publication**

683 Not applicable.

684 **Competing interests**

685 No competing interests.

686 **REFERENCES**

687 1. Sexton T, Cavalli G. The Role of Chromosome Domains in Shaping the Functional Genome. Cell. 2015
688 Mar 12;160(6):1049–59.

689 2. Hoencamp C, Dudchenko O, Elbatsh AMO, Brahmachari S, Raaijmakers JA, van Schaik T, et al. 3D
690 genomics across the tree of life reveals condensin II as a determinant of architecture type. Science.
691 2021 May 28;372(6545):984–9.

692 3. Lieberman-Aiden E, van Berkum NL, Williams L, Imakaev M, Ragoczy T, Telling A, et al.
693 Comprehensive Mapping of Long-Range Interactions Reveals Folding Principles of the Human
694 Genome. Science. 2009 Oct 9;326(5950):289–93.

695 4. Esposito A, Bianco S, Chiariello AM, Abraham A, Fiorillo L, Conte M, et al. Polymer physics reveals a
696 combinatorial code linking 3D chromatin architecture to 1D chromatin states. Cell Reports. 2022
697 Mar 29;38(13):110601.

698 5. Szalay MF, Majchrzycka B, Jerković I, Cavalli G, Ibrahim DM. Evolution and function of chromatin
699 domains across the tree of life. Nat Struct Mol Biol. 2024 Dec;31(12):1824–37.

700 6. Cremer T, Cremer C, Baumann H, Luedtke EK, Sperling K, Teuber V, et al. Rabl's model of the
701 interphase chromosome arrangement tested in Chinise hamster cells by premature chromosome
702 condensation and laser-UV-microbeam experiments. Hum Genet. 1982 Feb 1;60(1):46–56.

703 7. Álvarez-González L, Arias-Sardá C, Montes-Espuña L, Marín-Gual L, Vara C, Lister NC, et al. Principles
704 of 3D chromosome folding and evolutionary genome reshuffling in mammals. Cell Reports. 2022
705 Dec 20;41(12):111839.

706 8. Dong P, Tu X, Chu PY, Lü P, Zhu N, Grierson D, et al. 3D Chromatin Architecture of Large Plant
707 Genomes Determined by Local A/B Compartments. Mol Plant. 2017 Dec 4;10(12):1497–509.

708 9. Rao SSP, Huntley MH, Durand NC, Stamenova EK, Bochkov ID, Robinson JT, et al. A 3D map of the
709 human genome at kilobase resolution reveals principles of chromatin looping. Cell. 2014 Dec
710 18;159(7):1665–80.

711 10. Dixon JR, Selvaraj S, Yue F, Kim A, Li Y, Shen Y, et al. Topological Domains in Mammalian Genomes
712 Identified by Analysis of Chromatin Interactions. Nature. 2012 Apr 11;485(7398):376.

713 11. Long HS, Greenaway S, Powell G, Mallon AM, Lindgren CM, Simon MM. Making sense of the linear
714 genome, gene function and TADs. Epigenetics & Chromatin. 2022 Jan 29;15(1):4.

715 12. Flavahan WA, Drier Y, Liau BB, Gillespie SM, Venteicher AS, Stemmer-Rachamimov AO, et al.
716 Insulator dysfunction and oncogene activation in IDH mutant gliomas. Nature. 2016
717 Jan;529(7584):110–4.

718 13. Valton AL, Dekker J. TAD disruption as oncogenic driver. Current Opinion in Genetics &
719 Development. 2016 Feb 1;36:34–40.

720 14. Li E, Liu H, Huang L, Zhang X, Dong X, Song W, et al. Long-range interactions between proximal and
721 distal regulatory regions in maize. Nat Commun. 2019 June 14;10(1):2633.

722 15. Ricci WA, Lu Z, Ji L, Marand AP, Ethridge CL, Murphy NG, et al. Widespread long-range cis-regulatory
723 elements in the maize genome. Nat Plants. 2019 Dec;5(12):1237–49.

724 16. Dong P, Tu X, Liang Z, Kang BH, Zhong S. Plant and animal chromatin three-dimensional
725 organization: similar structures but different functions. J Exp Bot. 2020 Aug 17;71(17):5119–28.

726 17. Sun L, Zhou J, Xu X, Liu Y, Ma N, Liu Y, et al. Mapping nucleosome-resolution chromatin organization
727 and enhancer-promoter loops in plants using Micro-C-XL. Nat Commun. 2024 Jan 2;15(1):35.

728 18. Dame RT, Rashid FZM, Grainger DC. Chromosome organization in bacteria: mechanistic insights into
729 genome structure and function. Nat Rev Genet. 2020 Apr;21(4):227–42.

730 19. Le TBK, Imakaev MV, Mirny LA, Laub MT. High-resolution mapping of the spatial organization of a
731 bacterial chromosome. Science. 2013 Nov 8;342(6159):731–4.

732 20. Marbouty M, Cournac A, Flot JF, Marie-Nelly H, Mozziconacci J, Koszul R. Metagenomic
733 chromosome conformation capture (meta3C) unveils the diversity of chromosome organization in
734 microorganisms. Elife. 2014 Dec 17;3:e03318.

735 21. Cockram C, Thierry A, Gorlas A, Lestini R, Koszul R. Euryarchaeal genomes are folded into SMC-
736 dependent loops and domains, but lack transcription-mediated compartmentalization. Mol Cell.
737 2021 Feb 4;81(3):459-472.e10.

738 22. Takemata N, Bell SD. Multi-scale architecture of archaeal chromosomes. Mol Cell. 2021 Feb
739 4;81(3):473-487.e6.

740 23. Case NT, Gurr SJ, Fisher MC, Blehert DS, Boone C, Casadevall A, et al. Fungal impacts on Earth's
741 ecosystems. Nature. 2025 Feb;638(8049):49–57.

742 24. Engel SR, Dietrich FS, Fisk DG, Binkley G, Balakrishnan R, Costanzo MC, et al. The Reference Genome
743 Sequence of Saccharomyces cerevisiae: Then and Now. G3 (Bethesda). 2013 Dec 27;4(3):389–98.

744 25. Gupta YK, Marcelino-Guimarães FC, Lorrain C, Farmer A, Haridas S, Ferreira EGC, et al. Major
745 proliferation of transposable elements shaped the genome of the soybean rust pathogen
746 Phakopsora pachyrhizi. Nat Commun. 2023 Apr 1;14(1):1835.

747 26. Möller M, Stukenbrock EH. Evolution and genome architecture in fungal plant pathogens. Nat Rev
748 Microbiol. 2017 Dec;15(12):756–71.

749 27. Feurtey A, Lorrain C, Croll D, Eschenbrenner C, Freitag M, Habig M, et al. Genome
750 compartmentalization predates species divergence in the plant pathogen genus Zymoseptoria.
751 BMC Genomics. 2020 Aug 26;21(1):588.

752 28. Belton JM, McCord RP, Gibcus J, Naumova N, Zhan Y, Dekker J. Hi-C: A comprehensive technique to
753 capture the conformation of genomes. Methods. 2012 Nov;58(3):10.1016/j.ymeth.2012.05.001.

754 29. Torres DE, Reckard AT, Klocko AD, Seidl MF. Nuclear genome organization in fungi: from gene
755 folding to Rabl chromosomes. FEMS Microbiology Reviews. 2023 May 1;47(3):fuad021.

756 30. Yildirir G, Sperschneider J, Malar C M, Chen ECH, Iwasaki W, Cornell C, et al. Long reads and Hi-C
757 sequencing illuminate the two-compartment genome of the model arbuscular mycorrhizal
758 symbiont Rhizophagus irregularis. New Phytologist. 2022;233(3):1097–107.

759 31. Schalbetter SA, Fudenberg G, Baxter J, Pollard KS, Neale MJ. Principles of meiotic chromosome
760 assembly revealed in S. cerevisiae. Nat Commun. 2019 Oct 22;10(1):4795.

761 32. Torres DE, Kramer HM, Tracanna V, Fiorin GL, Cook DE, Seidl MF, et al. Implications of the three-
762 dimensional chromatin organization for genome evolution in a fungal plant pathogen. Nat
763 Commun. 2024 Feb 24;15(1):1701.

764 33. Galazka JM, Klocko AD, Uesaka M, Honda S, Selker EU, Freitag M. Neurospora chromosomes are
765 organized by blocks of importin alpha-dependent heterochromatin that are largely independent of
766 H3K9me3. Genome Res. 2016 Jan 8;26(8):1069–80.

767 34. Rodriguez S, Ward A, Reckard AT, Shtanko Y, Hull-Crew C, Klocko AD. The genome organization of
768 Neurospora crassa at high resolution uncovers principles of fungal chromosome topology. G3
769 Genes|Genomes|Genetics. 2022 May 1;12(5):jkac053.

770 35. Stukenbrock EH, Banke S, Javan-Nikkhah M, McDonald BA. Origin and Domestication of the Fungal
771 Wheat Pathogen Mycosphaerella graminicola via Sympatric Speciation. Molecular Biology and
772 Evolution. 2007 Feb 1;24(2):398–411.

773 36. Goodwin SB, M'Barek SB, Dhillon B, Wittenberg AHJ, Crane CF, Hane JK, et al. Finished Genome of
774 the Fungal Wheat Pathogen Mycosphaerella graminicola Reveals Dispensome Structure,
775 Chromosome Plasticity, and Stealth Pathogenesis. PLOS Genetics. 2011 June 9;7(6):e1002070.

776 37. Feurtey A, Lorrain C, McDonald MC, Milgate A, Solomon PS, Warren R, et al. A thousand-genome
777 panel retraces the global spread and adaptation of a major fungal crop pathogen. Nat Commun.
778 2023 Feb 24;14(1):1059.

779 38. Habig M, Quade J, Stukenbrock EH. Forward Genetics Approach Reveals Host Genotype-Dependent
780 Importance of Accessory Chromosomes in the Fungal Wheat Pathogen Zymoseptoria tritici. mBio.
781 2017 Nov 28;8(6):e01919-17.

782 39. Schotanus K, Soyer JL, Connolly LR, Grandaubert J, Happel P, Smith KM, et al. Histone modifications
783 rather than the novel regional centromeres of Zymoseptoria tritici distinguish core and accessory
784 chromosomes. Epigenetics & Chromatin. 2015 Oct 1;8(1):41.

785 40. Habig M, Lorrain C, Feurtey A, Komluski J, Stukenbrock EH. Epigenetic modifications affect the rate
786 of spontaneous mutations in a pathogenic fungus. Nat Commun. 2021 Dec;12(1):5869.

787 41. Möller M, Ridenour JB, Wright DF, Martin FA, Freitag M. H4K20me3 is important for Ash1-mediated
788 H3K36me3 and transcriptional silencing in facultative heterochromatin in a fungal pathogen. PLoS
789 Genet. 2023 Sept;19(9):e1010945.

42. Möller M, Habig M, Lorrain C, Feurtey A, Haueisen J, Fagundes WC, et al. Recent loss of the Dim2 DNA methyltransferase decreases mutation rate in repeats and changes evolutionary trajectory in a fungal pathogen. PLOS Genetics. 2021 Mar 22;17(3):e1009448.

43. Möller M, Schotanus K, Soyer JL, Haueisen J, Happ K, Stralucke M, et al. Destabilization of chromosome structure by histone H3 lysine 27 methylation. PLOS Genetics. 2019 avr;15(4):e1008093.

44. Möller M, Habig M, Freitag M, Stukenbrock EH. Extraordinary Genome Instability and Widespread Chromosome Rearrangements During Vegetative Growth. Genetics. 2018 Oct;210(2):517–29.

45. Lorrain C, Feurtey A, Möller M, Haueisen J, Stukenbrock E. Dynamics of transposable elements in recently diverged fungal pathogens: lineage-specific transposable element content and efficiency of genome defenses. G3 Genes|Genomes|Genetics. 2021 Apr 1;11(4):jkab068.

46. Meile L, Peter J, Puccetti G, Alassimone J, McDonald BA, Sánchez-Vallet A. Chromatin Dynamics Contribute to the Spatiotemporal Expression Pattern of Virulence Genes in a Fungal Plant Pathogen. mBio. 2020 Oct 6;11(5):10.1128/mbio.02343-20.

47. Badet T, Oggenfuss U, Abraham L, McDonald BA, Croll D. A 19-isolate reference-quality global pangenome for the fungal wheat pathogen Zymoseptoria tritici. BMC Biol. 2020 Dec;18(1):12.

48. Ortabozkoyun H, Huang PY, Gonzalez-Buendia E, Cho H, Kim SY, Tsirigos A, et al. Members of an array of zinc-finger proteins specify distinct *Hox* chromatin boundaries. Molecular Cell. 2024 Sept 19;84(18):3406-3422.e6.

49. Winter DJ, Ganley ARD, Young CA, Liachko I, Schardl CL, Dupont PY, et al. Repeat elements organise 3D genome structure and mediate transcription in the filamentous fungus Epichloë festucae. Richardson PM, editor. PLoS Genet. 2018 Oct 24;14(10):e1007467.

50. Shao W, Wang J, Zhang Y, Zhang C, Chen J, Chen Y, et al. The jet-like chromatin structure defines active secondary metabolism in fungi. Nucleic Acids Research. 2024 May 22;52(9):4906–21.

51. Davidse LC, Flach W. Differential binding of methyl benzimidazol-2-yl carbamate to fungal tubulin as a mechanism of resistance to this antimitotic agent in mutant strains of Aspergillus nidulans. J Cell Biol. 1977 Jan;72(1):174–93.

52. Goto B, Okazaki K, Niwa O. Cytoplasmic microtubular system implicated in de novo formation of a Rabl-like orientation of chromosomes in fission yeast. J Cell Sci. 2001 July;114(Pt 13):2427–35.

53. Jin QW, Fuchs J, Loidl J. Centromere clustering is a major determinant of yeast interphase nuclear organization. J Cell Sci. 2000 June;113 (Pt 11):1903–12.

54. Reckard AT, Pandeya A, Voris JM, Gonzalez Cruz CG, Oluwadare O, Klocko AD. A Constitutive Heterochromatic Region Shapes Genome Organization and Impacts Gene Expression in Neurospora crassa. bioRxiv. 2024 Oct 14;2024.06.07.597955.

55. Szalay MF, Majchrzycka B, Jerković I, Cavalli G, Ibrahim DM. Evolution and function of chromatin domains across the tree of life. Nat Struct Mol Biol. 2024 Nov 26;1–14.

826 56. Davidson IF, Barth R, Zaczek M, van der Torre J, Tang W, Nagasaka K, et al. CTCF is a DNA-tension-
827 dependent barrier to cohesin-mediated loop extrusion. Nature. 2023 Apr;616(7958):822–7.

828 57. Oberbeckmann E, Quililan K, Cramer P, Oudelaar AM. In vitro reconstitution of chromatin domains
829 shows a role for nucleosome positioning in 3D genome organization. Nat Genet. 2024
830 Mar;56(3):483–92.

831 58. Wing Shun Li, Lucas M Carter, L. Almassalha, Ruyi Gong, Emily M. Pujadas-Liwag, Tiffany Kuo, et al.
832 Mature chromatin packing domains persist after RAD21 depletion in 3D. Science Advances. 2025;

833 59. Trussart M, Yus E, Martinez S, Baù D, Tahara YO, Pengo T, et al. Defined chromosome structure in
834 the genome-reduced bacterium Mycoplasma pneumoniae. Nat Commun. 2017 Mar 8;8:14665.

835 60. Ramírez F, Bhardwaj V, Arrigoni L, Lam KC, Grüning BA, Villaveces J, et al. High-resolution TADs
836 reveal DNA sequences underlying genome organization in flies. Nature Communications. 2018 Jan
837 15;9(1):189.

838 61. Ortabozkoyun H, Huang PY, Gonzalez-Buendia E, Cho H, Kim SY, Tsirigos A, et al. Members of an
839 array of zinc-finger proteins specify distinct *Hox* chromatin boundaries. Molecular Cell. 2024 Sept
840 19;84(18):3406-3422.e6.

841 62. Liyakat Ali TM, Brunet A, Collas P, Paulsen J. TAD cliques predict key features of chromatin
842 organization. BMC Genomics. 2021 July 3;22(1):499.

843 63. Qian Bian, Bian Q, Erika Anderson, Anderson E, Qiming Yang, Yang Q, et al. Histone H3K9
844 methylation promotes formation of genome compartments in Caenorhabditis elegans via
845 chromosome compaction and perinuclear anchoring. Proceedings of the National Academy of
846 Sciences of the United States of America. 2020 May 8;117(21):11459–70.

847 64. Grob S, Schmid MW, Grossniklaus U. Hi-C Analysis in *Arabidopsis* Identifies the *KNOT*, a Structure
848 with Similarities to the *flamenco* Locus of *Drosophila*. Molecular Cell. 2014 Sept 4;55(5):678–93.

849 65. Sun L, Jing Y, Liu X, Li Q, Xue Z, Cheng Z, et al. Heat stress-induced transposon activation correlates
850 with 3D chromatin organization rearrangement in Arabidopsis. Nat Commun. 2020 Apr
851 20;11(1):1886.

852 66. Bolger AM, Lohse M, Usadel B. Trimmomatic: a flexible trimmer for Illumina sequence data.
853 Bioinformatics. 2014 Aug 1;30(15):2114–20.

854 67. Wingett S, Ewels P, Furlan-Magaril M, Nagano T, Schoenfelder S, Fraser P, et al. HiCUP: pipeline for
855 mapping and processing Hi-C data. F1000Res. 2015 Nov 20;4:1310.

856 68. Vasimuddin Md, Misra S, Li H, Aluru S. Efficient Architecture-Aware Acceleration of BWA-MEM for
857 Multicore Systems. In: 2019 IEEE International Parallel and Distributed Processing Symposium
858 (IPDPS) [Internet]. 2019 [cited 2025 Feb 14]. p. 314–24. Available from:
859 https://ieeexplore.ieee.org/document/8820962

860 69. Krzywinski MI, Schein JE, Birol I, Connors J, Gascoyne R, Horsman D, et al. Circos: An information
861 aesthetic for comparative genomics. Genome Res [Internet]. 2009 June 18 [cited 2025 Feb 14];
862 Available from: https://genome.cshlp.org/content/early/2009/06/15/gr.092759.109

863 70. Open2C, Abdennur N, Abraham S, Fudenberg G, Flyamer IM, Galitsyna AA, et al. Cooltools: Enabling
864 high-resolution Hi-C analysis in Python. PLOS Computational Biology. 2024 May 6;20(5):e1012067.

865 71. Sanborn AL, Rao SSP, Huang SC, Durand NC, Huntley MH, Jewett AI, et al. Chromatin extrusion
866 explains key features of loop and domain formation in wild-type and engineered genomes. Proc
867 Natl Acad Sci U S A. 2015 Nov 24;112(47):E6456-6465.

868 72. Kleiber C, Zeileis A. Diagnostics and Alternative Methods of Regression. In: Kleiber C, Zeileis A,
869 editors. Applied Econometrics with R [Internet]. New York, NY: Springer; 2008 [cited 2025 Apr 25].
870 p. 1–27. Available from: https://doi.org/10.1007/978-0-387-77318-6_4

871 73. Wickham H. ggplot2 [Internet]. Cham: Springer International Publishing; 2016 [cited 2025 Apr 25].
872 (Use R!). Available from: http://link.springer.com/10.1007/978-3-319-24277-4

873 74. Lapalu N, Lamothe L, Petit Y, Genissel A, Delude C, Feurtey A, et al. Improved gene annotation of the
874 fungal wheat pathogen *Zymoseptoria tritici* based on combined Iso-Seq and RNA-Seq evidence
875 [Internet]. Genomics; 2023 Apr [cited 2024 Mar 7]. Available from:
876 http://biorxiv.org/lookup/doi/10.1101/2023.04.26.537486

877 75. Miñana-Posada S, Lorrain C, McDonald BA, Feurtey A. Thermal adaptation in worldwide collections
878 of a major fungal pathogen [Internet]. bioRxiv; 2024 [cited 2024 Nov 14]. p. 2024.09.12.612681.
879 Available from: https://www.biorxiv.org/content/10.1101/2024.09.12.612681v1

880 76. topGO [Internet]. Bioconductor. 2024 [cited 2024 Aug 1]. Available from:
881 http://bioconductor.org/packages/topGO/

882 77. Baril T, Croll D. A pangenome-guided manually curated library of transposable elements for
883 Zymoseptoria tritici. BMC Research Notes. 2023 Nov 16;16(1):335.

884 78. Sandelin A, Alkema W, Engström P, Wasserman WW, Lenhard B. JASPAR: an open-access database
885 for eukaryotic transcription factor binding profiles. Nucleic Acids Research. 2004 Jan
886 1;32(suppl_1):D91–4.

887 79. MEME Suite: tools for motif discovery and searching | Nucleic Acids Research | Oxford Academic
888 [Internet]. [cited 2025 Feb 19]. Available from:
889 https://academic.oup.com/nar/article/37/suppl_2/W202/1135092

890 80. Gu Z, Eils R, Schlesner M, Ishaque N. EnrichedHeatmap: an R/Bioconductor package for
891 comprehensive visualization of genomic signal associations. BMC Genomics. 2018 Apr 4;19(1):234.

892 81. Haueisen J, Möller M, Eschenbrenner CJ, Grandaubert J, Seybold H, Adamiak H, et al. Highly flexible
893 infection programs in a specialized wheat pathogen. Ecol Evol. 2018 Dec 26;9(1):275–94.

894 82. Dobin A, Davis CA, Schlesinger F, Drenkow J, Zaleski C, Jha S, et al. STAR: ultrafast universal RNA-seq
895 aligner. Bioinformatics. 2013 Jan;29(1):15–21.

896 83. Jin Y, Tam OH, Paniagua E, Hammell M. TEtranscripts: a package for including transposable elements
897 in differential expression analysis of RNA-seq datasets. Bioinformatics. 2015 Nov 15;31(22):3593–
898 9.

899 84. Love MI, Huber W, Anders S. Moderated estimation of fold change and dispersion for RNA-seq data
900 with DESeq2. Genome Biology. 2014 Dec 5;15(12):550.

901 85. Langmead B, Salzberg SL. Fast gapped-read alignment with Bowtie 2. Nat Methods. 2012
902 Apr;9(4):357–9.

903 86. Morrissey A, Shi J, James DQ, Mahony S. Accurate allocation of multimapped reads enables
904 regulatory element analysis at repeats. Genome Res. 2024 June;34(6):937–51.

905 87. Picard Tools - By Broad Institute [Internet]. [cited 2025 Feb 19]. Available from:
906 https://broadinstitute.github.io/picard/

907 88. Krueger F, Andrews SR. Bismark: a flexible aligner and methylation caller for Bisulfite-Seq
908 applications. Bioinformatics. 2011 June 1;27(11):1571–2.

909 89. Minana-Posada S, Feurtey A, Alassimone J, McDonald BA, Lorrain C. Responses to temperature
910 shocks in Zymoseptoria tritici reveal specific transcriptional reprogramming and novel candidate
911 genes for thermal adaptation [Internet]. bioRxiv; 2024 [cited 2025 Feb 19]. p. 2024.12.16.628617.
912 Available from: https://www.biorxiv.org/content/10.1101/2024.12.16.628617v1

913

914 **LEGENDS**

915 **Fig. 1: The Rabl-like three-dimensional structure of *Zymoseptoria tritici* is compartmentalized**. a)
916 Heatmap of genome-wide normalized Hi-C contact map at 10kb resolution. Contact numbers per 10kb
917 bins are represented in a log scale. Chromosomes are represented by ideograms with purple marking the
918 centromeres [39]. b) Strongest inter-chromosomal interactions with an observed-to-expected value >3.5
919 at 10 kb bin resolution. Core chromosomes are represented in light blue. Accessory chromosomes are
920 represented in dark blue. Centromeres are marked by triangles. H3K9me3 enrichment is shown in the
921 orange histogram. Links represent inter-chromosomal pericentromere-pericentromere interactions
922 (purple), accessory-core chromosome (green), or any other interactions (grey). c) Contact probability (top)
923 and contact frequency decay slope (bottom) against genomic distance for core (green) and accessory
924 (orange) chromosomes. d) Relationship between chromosomal interaction strength and chromosome loss

925 in *Zymoseptoria tritici* strain IPO323, after carbendazim treatment [38]. Scatterplot showing the
926 association between log-transformed normalized Hi-C interaction strength (x-axis) and the frequency of
927 chromosome loss (y-axis) across individual chromosomes. A dashed grey line indicates the predicted linear
928 relationship. The model indicates a significant inverse relationship between interaction strength and
929 chromosome loss (Poisson GLM, p-value < 0.05).
930
931 **Fig. 2: Homotypic interactions and epigenomic features of A/B compartments in the *Zymoseptoria tritici***
932 **genome.** a) Saddle plot representing genome-wide intrachromosomal Hi-C interactions at 3 kb resolution.
933 Homotypic B-B interactions are represented in the top-left, while A-A interactions are observed in the
934 bottom-right. b) Enrichment of histone modifications across A and B compartments, highlighting distinct
935 chromatin states. c) Genomic composition of A and B compartments, showing proportions of genes
936 (green), transposable elements (orange), and intergenic regions (grey). d) Density of genes (green) and
937 transposable elements (orange) across A and B compartments. e) Distribution of transposable element
938 families within A and B compartments. Asterisks indicate statistically significant differences in TE content
939 based on pairwise Fisher exact tests with FDR correction using the Benjamin-Hochberg method (ns: non-
940 significant; *: p-value < 0.05; **: p-value < 0.01; ***: p-value < 0.001). f) *In vitro* Expression levels of genes
941 (green) and transposable elements (orange) in A and B compartments.
942
943 **Fig. 3: The genome of *Zymoseptoria tritici* forms chromatin interacting domains (CIDs) with specific**
944 **genomic and epigenomic signatures.** a) Close-up of Hi-C contact map showing local interaction
945 frequencies at 3 kb bins resolution and detection of self-interacting CID structures. Insulation score was
946 calculated with a genome-wide sliding window approach. Predicted CIDs are represented by black
947 triangles, and boundaries are indicated by red arrows. b) Heatmap of chromatin insulation scores, histone
948 modifications (H3K36me3 and H3K9me3), gene, and TE density enrichment centered on domain

949 boundaries, with 35 kb upstream and downstream regions shown per row. The top panel shows the
950 average profile across all boundaries depicted in the heatmap. c) Close-up example of CID annotations on
951 chromosome 4 of *Z. tritici* IPO323. From top to bottom: strongest intra-chromosomal links
952 (observed/expected > 1.75) across chromosome 4; chromosome 4 Hi-C contact map with CID annotated
953 by triangles; insulation scores within chromosome 4; histone modifications for euchromatin H3K4me2,
954 heterochromatin H3K9me2, H3K9me3, and facultative heterochromatin H3K27me2, H3K27me3,
955 H3K36me3, H3K20me1, H4K20me3. d) Heatmap of chromatin insulation scores, histone modifications, 5-
956 methylcytosine DNA methylation (5mC), repeat-induced point mutation (RIP) composite index frequency,
957 genes, and TEs density centered on CIDs, with 35 kb upstream and downstream regions shown per row.
958 The top panel shows the average profile across all CIDs depicted in the heatmap. Highly-insulated CIDs
959 (HI-CIDs) are depicted by solid lines, and "regular-CIDs" (R-CIDs) are depicted by dashed lines.
960
961 **Supplementary Fig. S1: Quality assessment of the Hi-C libraries replicates.** a) Pearson correlation
962 between Hi-C contact map replicates in *Zymoseptoria tritici* IPO323 (Pearson correlation = 0.87). b) Hi-C
963 libraries quality filtering with the HiCUP-0.9.2 [67] pipeline.
964
965 **Supplementary Fig. S2: *Zymoseptoria tritici* IPO323 Hi-C contact map 10kb bins normalized per genomic**
966 **distance as observed/expected interactions.**
967
968 **Supplementary Fig. S3: Strongest interactions in *Zymoseptoria tritici* IPO323.** Links represent the
969 strongest interactions with observed-to-expected values >3.5 at 10 kb bin resolution for a) all strong
970 interactions, b) inter-chromosomal pericentromere-pericentromere interactions, c) accessory-core
971 chromosome interactions with inter-chromosomal pericentromere-pericentromere interactions (purple),

972 accessory-core chromosome (green), H3K9me3-H3K9me3 interactions (orange) or any other interactions
973 (grey), d) H3K9me3-H3K9me3 interactions.
974
975 **Supplementary Fig. S4: Interchromosomal compartmentalization in *Zymoseptoria tritici* IPO323.** a) Self-
976 interacting compartments were identified from Hi-C contact matrix at 10 kb resolution. Principal
977 component analysis (PCA) of interchromosomal contact frequencies was used to extract the first
978 eigenvector (E1), with positive and negative values annotated in yellow and purple, respectively. The
979 eigenvector track is shown above each panel. The Hi-C contact map with 10 kb resolution is shown for all
980 chromosomes, shown by ideograms on the side, with centromeres represented in purple. b) Saddle plot
981 representing genome-wide Hi-C interactions at 10 kb resolution. Homotypic interactions between regions
982 associated with a negative E1 are represented in the top-left, while positive E1 region interactions are
983 observed in the bottom-right.
984
985 **Supplementary Fig. S5: Intrachromosomal A/B compartments in *Zymoseptoria tritici* IPO323.** For each
986 chromosome, A/B compartments were identified from Hi-C contact matrices at 10 kb resolution. Principal
987 component analysis (PCA) of intrachromosomal contact frequencies was used to extract the first
988 eigenvector (E1), with positive and negative values corresponding to A (yellow) and B (purple)
989 compartments, respectively. The eigenvector track is shown above each panel. Enrichment of H3K9me3
990 per 10 kb window is displayed as a histogram below the eigenvector track. Hi-C contact maps are shown
991 for individual chromosomes. Centromeres are represented by yellow stars.
992
993 **Supplementary Fig. S6: Chromatin interacting domain (CID) boundaries characteristics in core and**
994 **accessory chromosomes of *Zymoseptoria tritici* IPO323.** Heatmaps of chromatin insulation scores,
995 enrichment in histone modifications (H3K4me2, H3K9me2, H3K9me3, H3K27me2, H3K27me3,

996 H3K36me3, H4K20me1, H4K20me3), 5-methylcytosine DNA methylation (5mC), repeat-induced point
997 mutation (RIP) composite index frequency, genes, and TEs density centered on domain boundaries, with
998 35 kb upstream and downstream regions shown per row. The top panel shows the average profile across
999 core (solid lines) and accessory (dash lines) chromosomes boundaries depicted in the heatmap.
1000
1001 **Supplementary Fig. S7: *In vitro* Expression levels of genes and transposable elements in chromatin**
1002 **interacting domains (CIDs) and boundaries.** a) Violin plots (left) show log_2-transformed expression levels
1003 (log_2 RPKM+1) for genes (green) and TEs (orange) located within CIDs or at CID boundaries under axenic
1004 culture conditions. The heatmap (right) shows normalized gene expression centered on CID boundaries,
1005 with 35 kb upstream and downstream per row. The top panel displays the average log_2(RPKM+1) profile
1006 across all boundaries. b) Violin plots (left) show the absolute log_2 fold-change in gene and TE expression
1007 (infection vs. axenic) for elements within CIDs or at boundaries. The heatmap (right) shows absolute
1008 expression changes centered on CID boundaries (±35 kb), with the top panel showing the average profile.
1009 Statistical significance of differences between CIDs and boundaries was assessed using a two-sided Mann-
1010 Whitney U test with asterisks indicating significance levels with asterisks indicating significance levels (ns:
1011 non-significant).
1012
1013 **Supplementary Fig. S8: Strongest interactions between chromatin interacting domain (CIDs).**
1014 Distribution of observed-to-expected contact ratios > 1.75 from the 10 kb resolution interaction matrix,
1015 highlighting the strongest intrachromosomal interactions classified as either highly insulated CIDs (HI-
1016 CIDs) or regular CIDs (R-CIDs). Statistical significance of differences between groups was assessed using a
1017 two-sided Mann-Whitney U test with asterisks indicating significance levels (ns: non-significant; *: p-value
1018 < 0.05; **: p-value < 0.01; ***: p-value < 0.001).
1019

1020 **Supplementary Fig. S9: *In vitro* Expression levels of genes in regular chromatin interacting domains (R-**
1021 **CIDs) and highly insulated chromatin interacting domains (HI-CIDs).** Genes are represented in green and
1022 transposable elements in orange. Statistical significance of differences between HI-CIDs and R-CIDs was
1023 assessed using a two-sided Mann-Whitney U test with asterisks indicating significance levels (ns: non-
1024 significant; *: p-value < 0.05; **: p-value < 0.01; ***: p-value < 0.001).
1025
1026 **Supplementary Fig. S10: Co-regulated chromatin interacting domains (CIDs) during wheat infection**
1027 **stages.** Effect sizes from linear regression models quantified the contribution of each topologically
1028 associating domain (CID) to differential gene expression between in vitro growth on YMA medium and
1029 various in planta infection stages (stage A: early biotrophic, stage B: late biotrophic, stage C: early
1030 necrotrophic, and stage D: late necrotrophic). Each point represents the mean effect size per CID,
1031 accompanied by a 95% confidence interval. CIDs with statistically significant effects (i.e., confidence
1032 intervals not overlapping zero) are highlighted in color and annotated with their chromosome and CID
1033 identifiers. Values reflect normalized means derived from two independent biological replicates [81].
1034
1035 **Supplementary Fig. S11: Overlap between chromatin interacting domain (CID) categories.** Venn diagram
1036 illustrating the overlap among three categories of topology-associated domains (CIDs): co-regulated CIDs
1037 (defined as containing ≥10 genes or transposable elements with coordinated expression), highly insulated
1038 CIDs (HI-CIDs; identified by elevated insulation scores), and accessory chromosome CIDs (located on
1039 accessory chromosomes).
1040
1041 **Supplementary Fig. S12: Validation of CID boundary predictions based on intra-domain interaction**
1042 **frequencies.** Boxplots show the average intra-domain interaction frequency for annotated CIDs ("Original
1043 CID") compared to control regions of identical size shifted upstream or downstream by half the domain

1044 length (two-sided Mann-Whitney U test with asterisks indicating significance levels (ns: non-significant; *:

1045 p-value < 0.05).

1046

1047 **Supplementary Table S1: Quality assessment of Hi-C sequencing data.**

1048 **Supplementary Table S2: Hi-C matrix contact coverage per chromosome.**

1049 **Supplementary Table S3: Strongest interchromosomal interactions.** Hi-C interactions were normalized

1050 in observed vs expected (o/e) contacts.

1051 **Supplementary Table S4: Contact frequency decay exponent per chromosome.**

1052 **Supplementary Table S5: A/B compartments from PCA eigenvector analysis.**

1053 **Supplementary Table S6: Gene/TE content of A/B compartments.**

1054 **Supplementary Table S7: TE content of A/B compartments.**

1055 **Supplementary Table S8: Gene ontology enrichment in A compartment.**

1056 **Supplementary Table S9: Gene ontology enrichment in B compartment.**

1057 **Supplementary Table S10: Chromatin interacting domains (CIDs (CIDs) annotation in the *Z. tritici* IPO323**

1058 **genome.**

1059 **Supplementary Table S11: CID boundaries annotations in the *Z. tritici* IPO323 genome.**

1060 **Supplementary Table S12: CIDs summary metrics in core and accessory chromosomes.**

1061 **Supplementary Table S13: Core orthologous genes enrichment in CID boundaries.** The core orthologous

1062 genes are present in 19 reference genomes of *Z. tritici* [47,89].

1063 **Supplementary Table S14: PFAM domains enrichment in CID boundaries.**

1064 **Supplementary Table S15: Gene ontology enrichment in CID boundaries.**

1065 **Supplementary Table S16: Motifs enrichment in CID boundaries.**

1066 **Supplementary Table S17: ZNF263 BLASTp searches in *Zymoseptoria tritici* IPO323 proteome**

1067 **Supplementary Table S18: Annotation of highly insulated CIDs (HI-CIDs) and regular CIDs (R-CIDs).**

1068 **Supplementary Table S19: Effector gene enrichment in highly insulated CIDs (HI-CIDs)**

1069 **Supplementary Table S20: Gene/TE expression analysis *in planta* stage A (early biotrophic phase)**

1070 **versus *in vitro*.**

1071 **Supplementary Table S21: Gene/TE expression analysis *in planta* stage B (late biotrophic phase) versus**

1072 ***in vitro*.**

1073 **Supplementary Table S22: Gene/TE expression analysis *in planta* stage C (early necrotrophic phase)**

1074 **versus *in vitro*.**

1075 **Supplementary Table S23: Gene/TE expression analysis *in planta* stage D (late necrotrophic phase)**

1076 **versus *in vitro*.**

1077 **Supplementary Table S24: Table S23: Linear models for CID co-expression analyses.**

1078 **Supplementary Table S25: Summary metrics of co-regulated CIDs.**

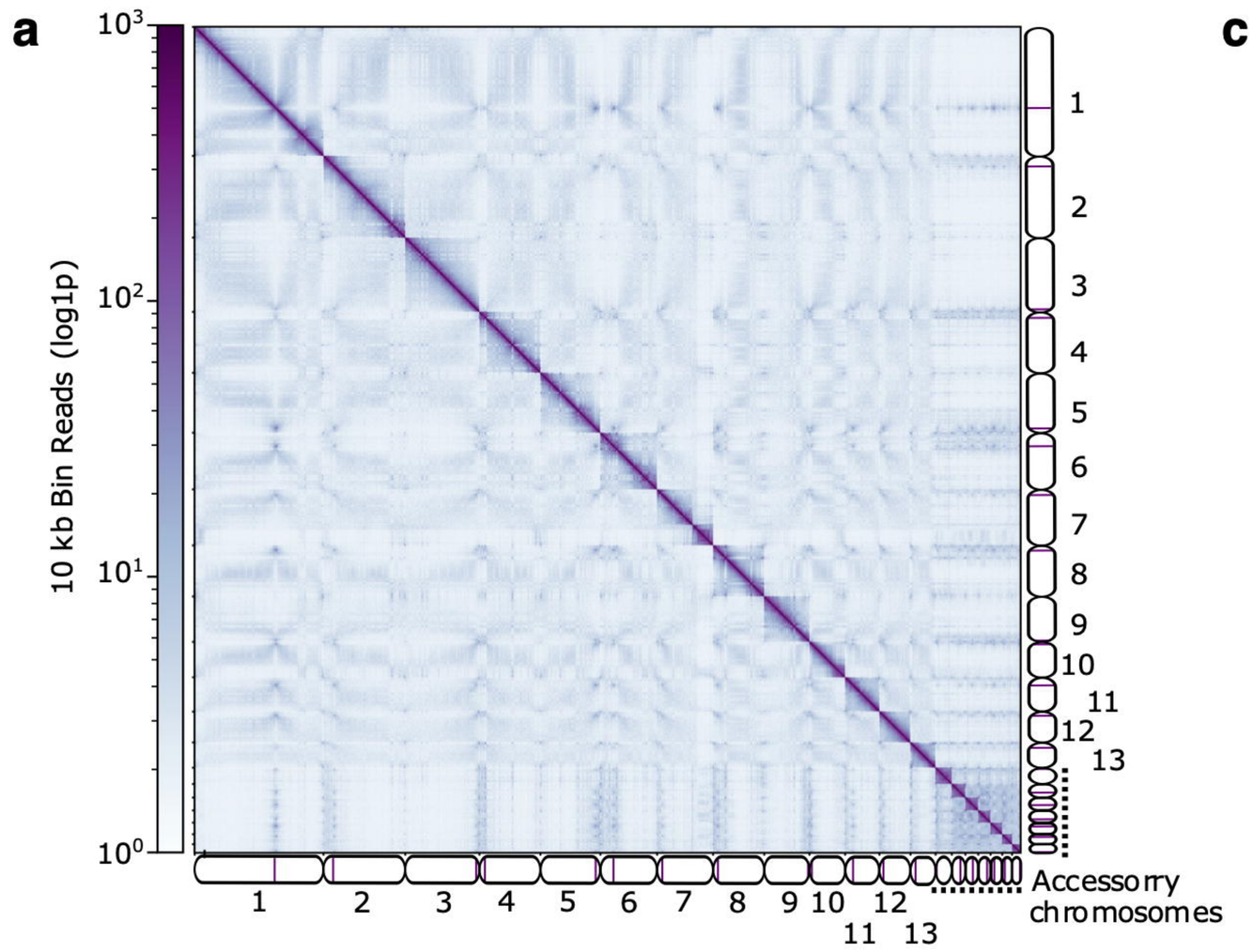
a
10 kb Bin Reads (log1p)
Accessorry chromosomes

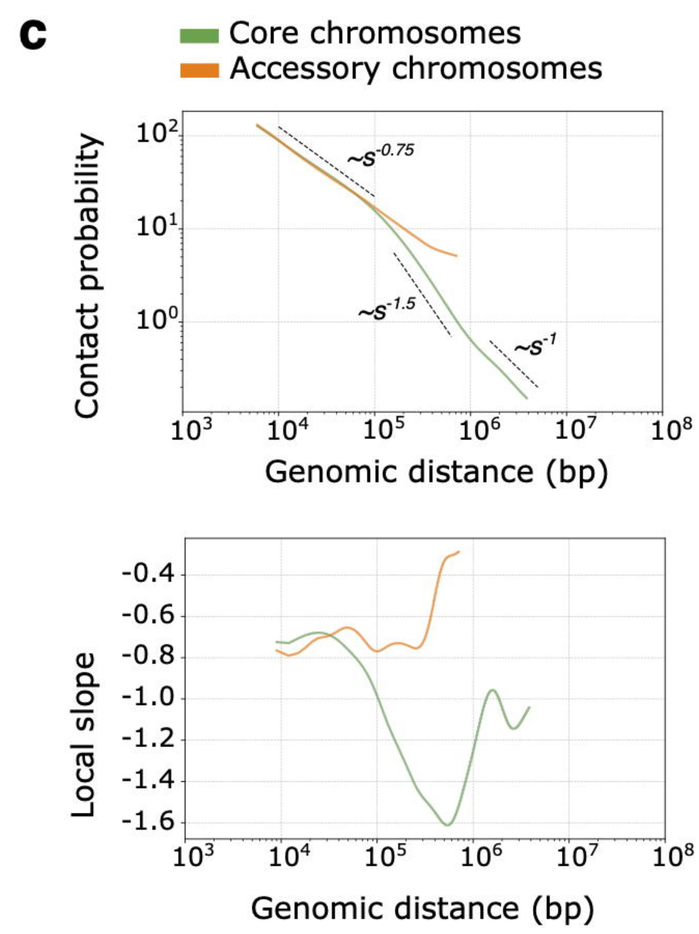
c
Core chromosomes
Accessory chromosomes
Contact probability
Genomic distance (bp)
Local slope
Genomic distance (bp)

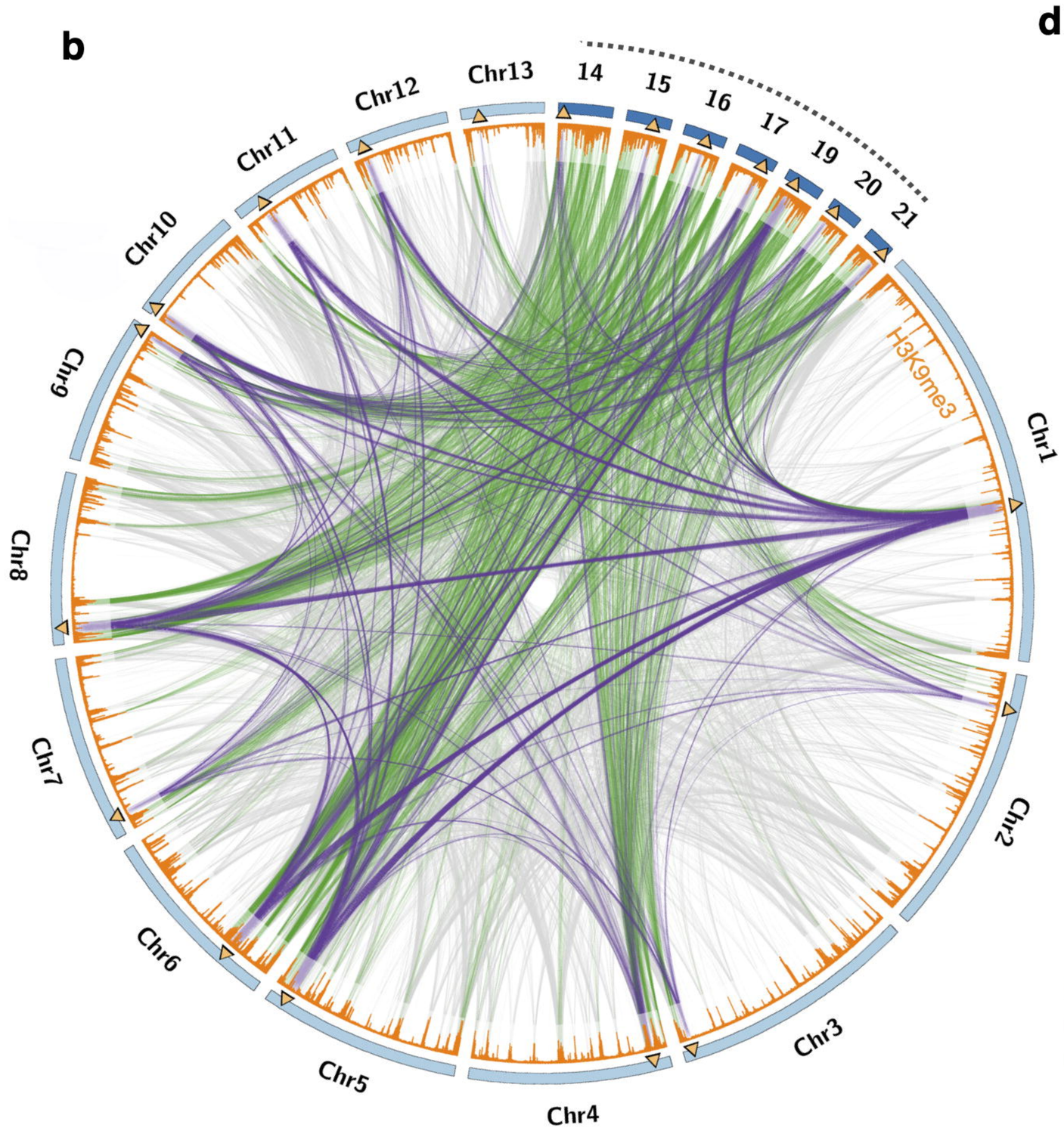
b
H3K9me3
Centromeres
Pericentromere-pericentromere links
Accessory-core chromosome links
Other links

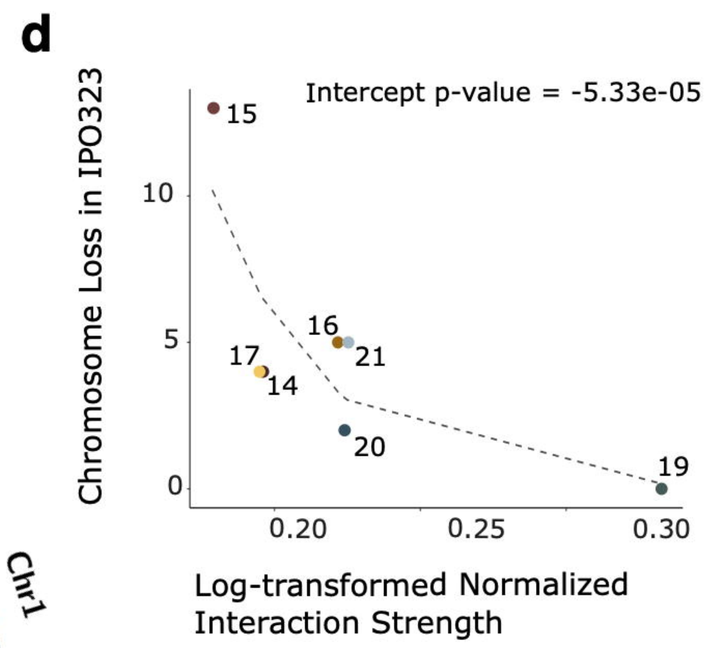
d
Intercept p-value = -5.33e-05
Chromosome Loss in IPO323
Log-transformed Normalized Interaction Strength

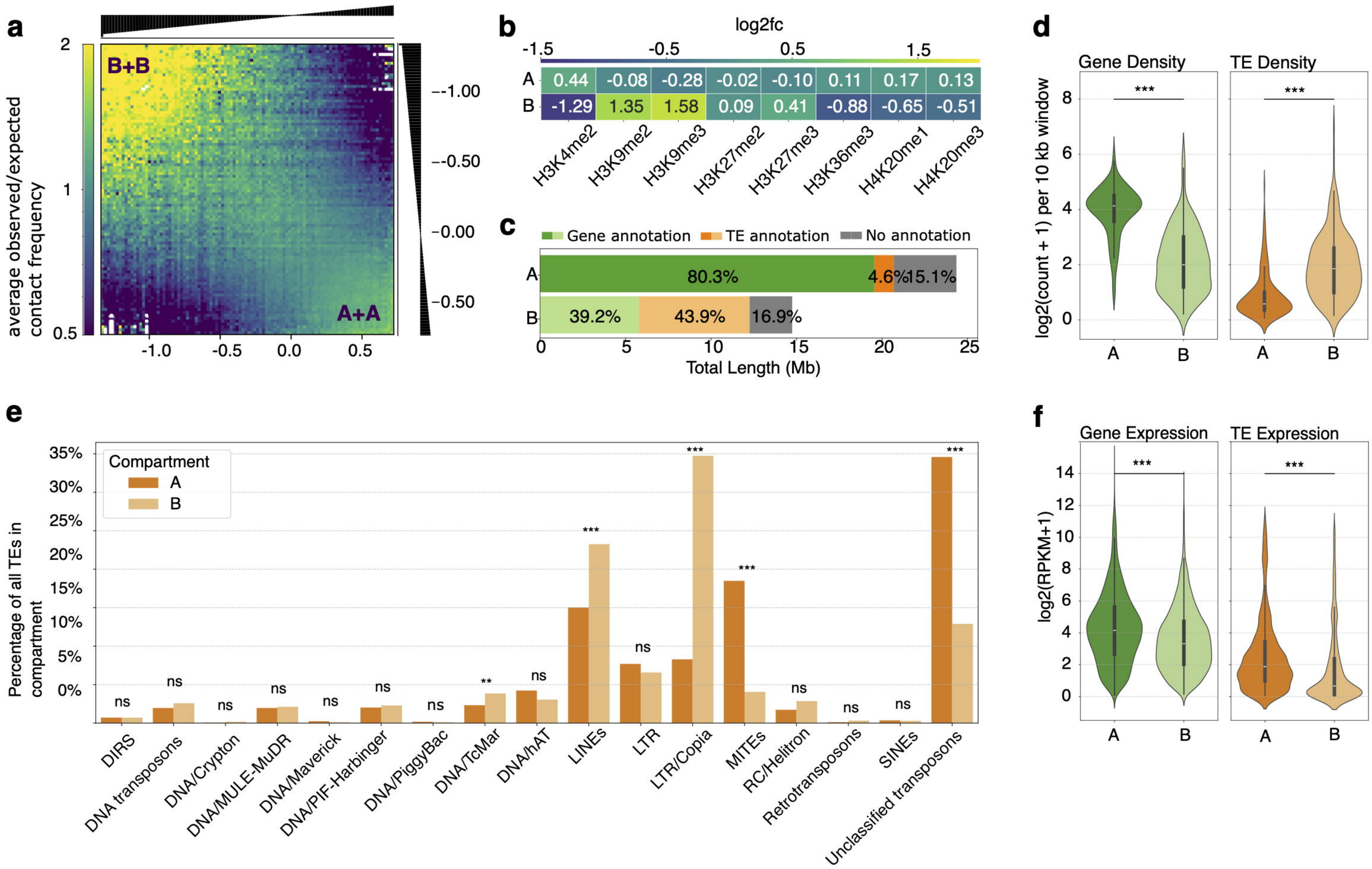
a
B+B
A+A
average observed/expected contact frequency
b
log2fc
A 0.44 -0.08 -0.28 -0.02 -0.10 0.11 0.17 0.13
B -1.29 1.35 1.58 0.09 0.41 -0.88 -0.65 -0.51
H3K4me2
H3K9me2
H3K9me3
H3K27me2
H3K27me3
H3K36me3
H4K20me1
H4K20me3
c
Gene annotation
TE annotation
No annotation
80.3% 4.6% 15.1%
39.2% 43.9% 16.9%
Total Length (Mb)
d
Gene Density
TE Density
log2(count + 1) per 10 kb window
e
Compartment
A
B
Percentage of all TEs in compartment
DIRS
DNA transposons
DNA/Crypton
DNA/MULE-MuDR
DNA/Maverick
DNA/PIF-Harbinger
DNA/PiggyBac
DNA/TcMar
DNA/hAT
LINEs
LTR
LTR/Copia
MITEs
RC/Helitron
Retrotransposons
SINEs
Unclassified transposons
f
Gene Expression
TE Expression
log2(RPKM+1)

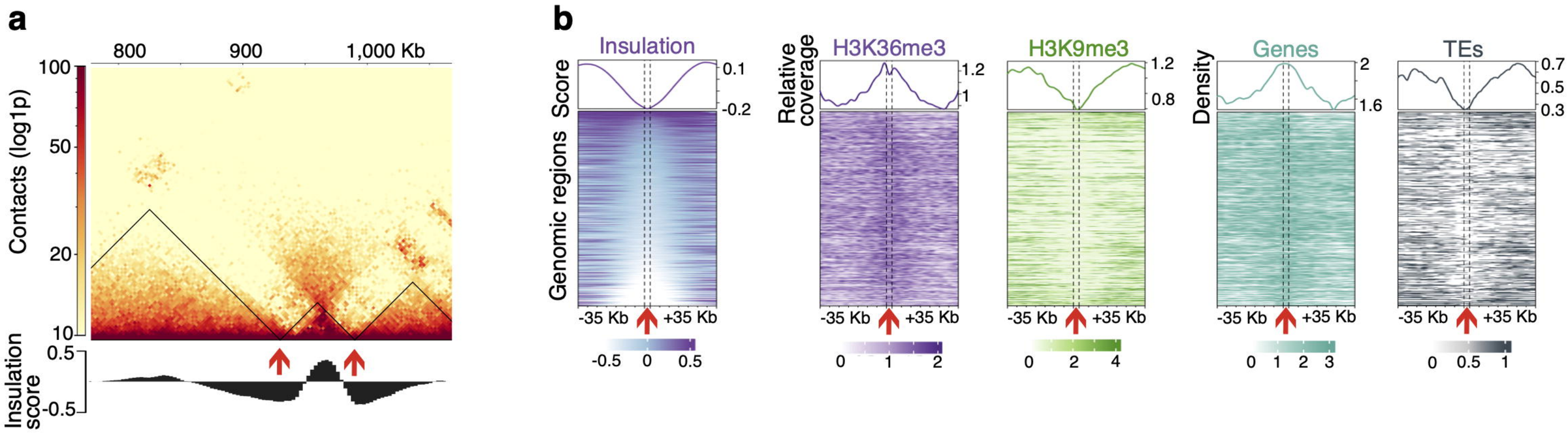
a
800
900
1,000 Kb
Contacts (log1p)
Insulation score
b
Insulation
H3K36me3
H3K9me3
Genes
TEs
Score
Relative coverage
Density
Genomic regions
-35 Kb
+35 Kb

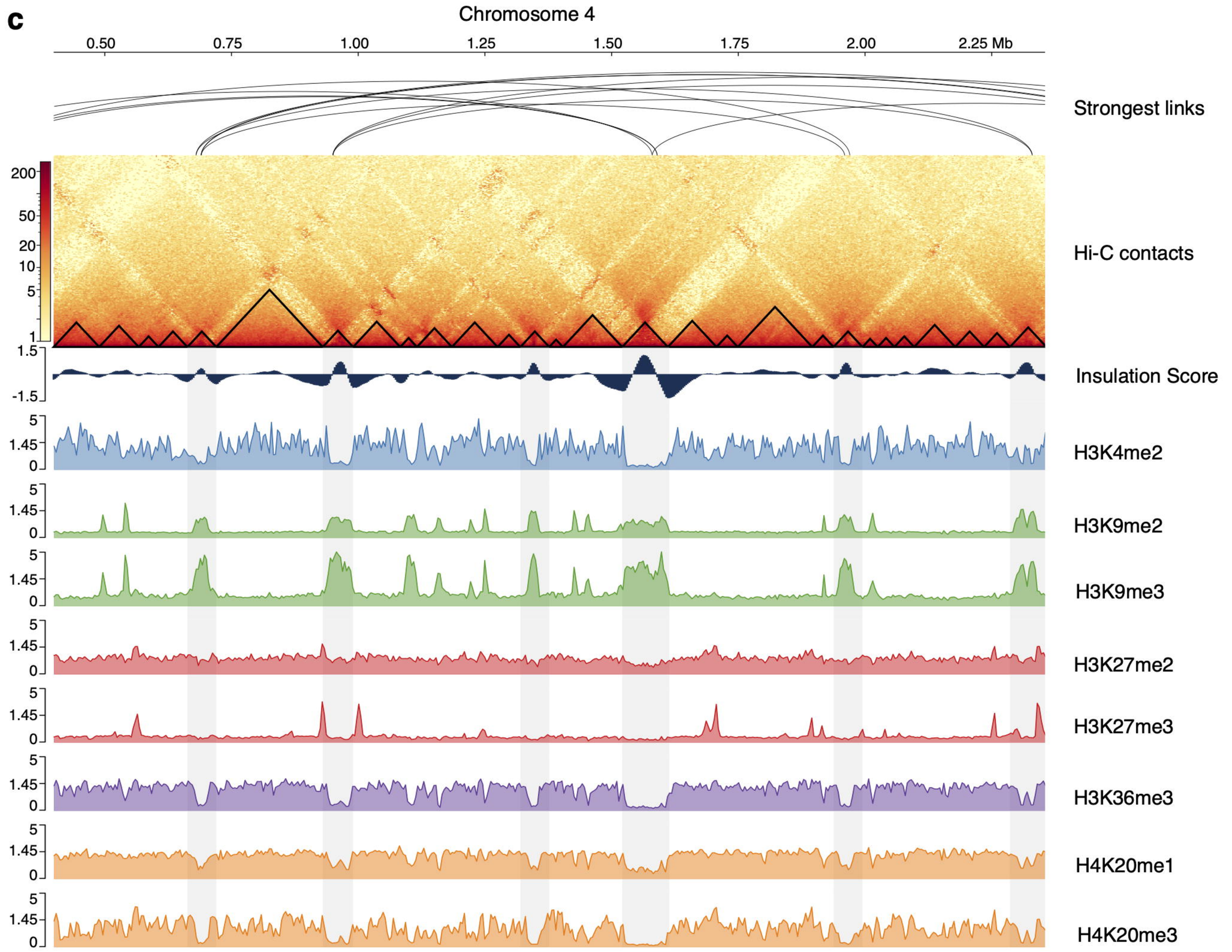
c
Chromosome 4
0.50
0.75
1.00
1.25
1.50
1.75
2.00
2.25 Mb
Strongest links
Hi-C contacts
Insulation Score
H3K4me2
H3K9me2
H3K9me3
H3K27me2
H3K27me3
H3K36me3
H4K20me1
H4K20me3

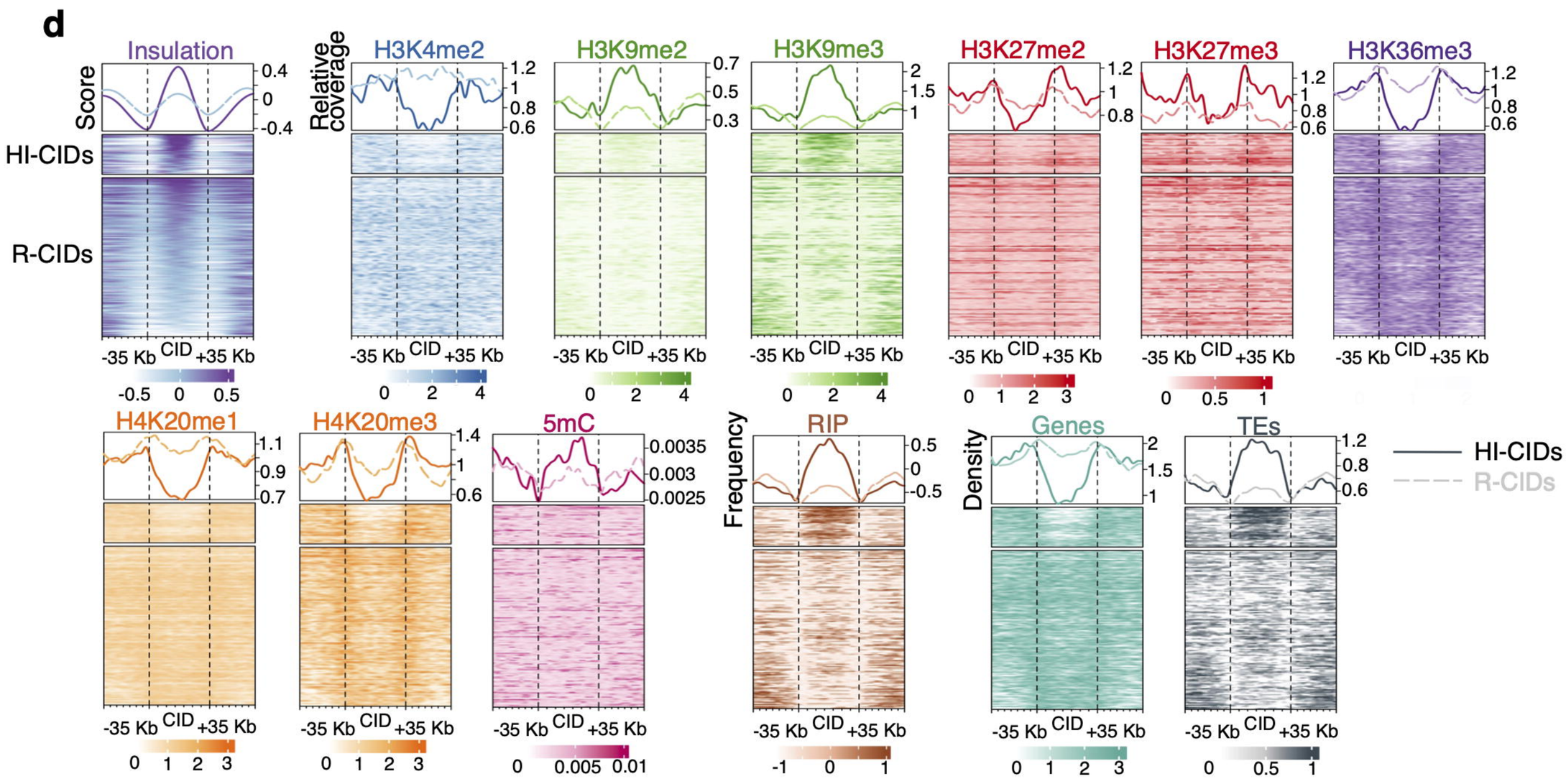
d
Insulation
H3K4me2
H3K9me2
H3K9me3
H3K27me2
H3K27me3
H3K36me3
Score
Relative coverage
HI-CIDs
R-CIDs
-35 Kb
CID
+35 Kb
H4K20me1
H4K20me3
5mC
RIP
Genes
TEs
Frequency
Density
HI-CIDs
R-CIDs